Progress In Electromagnetics Research B, Vol. 74, 37–59, 2017

Evaluation of Forces and Torques Generated by Toroidal Helicoidal Magnetic Fields

Roberto Muscia*

Abstract—In this paper, the computation of forces and torques mutually applied between a helical toroidal magnet and a magnet shaped like an angular plane sector is illustrated. The evaluation considers the magnetostatic field hypothesis. The main aim of this study is to present a tool for performing fast and accurate evaluation of forces and torques based on the method of the magnetic charges referring to helical toroidal magnetic systems. The particular geometry of the case study concerns the development of unconventional configurations of electrical machines. These configurations should reduce the magnetic flux changing during the machine operation. A small change of the magnetic flux reduces all the losses related to the flux variation. The illustrated model for the computation of forces and moments also shows a starting point for a reliable analytical numerical evaluation of the external/internal actions applied to parts of other kinds of helical toroidal systems as *stellarator* and similar ones.

1. INTRODUCTION

Efficiency depends on several factors, and the geometric configuration of an electrical machine usually significantly affects the performance. For reasons of manufacturing simplicity and rationality, two kinds of electric machines are usually designed and manufactured: those with a rotational degree of freedom (the traditional electric generators/motors) and those with a translation degree of freedom (electromechanical linear actuators). The performance of these devices is not always high in both cases. Factors related to the i) nonlinear magnetization characteristic [1–3], ii) non-linear demagnetization of permanent magnets [4, 5], and iii) saturation effects reduce the efficiency. These phenomena also depend on the geometric configuration of the device. Consequently, as discussed in [6], the attempt for evaluating if there are other possible architectures for magnetic systems that minimize the previously mentioned negative effects of the factors i), ii), and iii) can be beneficial. Therefore, with reference to the development of new configurations of electrical machines, a toroidal helicoidal arrangement of permanent magnets has been considered.

In order to perform quick and accurate evaluation of the performance of such devices, it is important to evaluate forces and torques that the helical toroidal permanent magnet applies to the moving permanent magnets. Before we illustrate the mathematical physical model developed to evaluate forces and torques, a short description of the magnetic system is given. The system has already been partially described in [6], but for the convenience of the reader, its working principle is summarized in the following. We can also see that the knowledge of forces and moments caused by this particular configuration of the magnetic field can be advantageous not only when searching for new configurations of electrical machines with high efficiency. Actually, the model for the computation of forces and moments illustrated in the following also represents a starting point for a reliable analytical numerical evaluation of the external/internal actions applied to other kinds of helical toroidal system. In these systems, synchrotron light sources [7], *tokamaks* [8–12], *stellarator* [13–17], and *hybrid tokamak-stellarator* [18],

Received 11 October 2016, Accepted 28 February 2017, Scheduled 6 April 2017
* Corresponding author: Roberto Muscia (muscia@units.it).
The author is with the University of Trieste, Department of Engineering and Architecture, Trieste, Italy.

magnetic forces are applied to electrical helicoidal coils. In order to ensure a good structural strength of such devices, these forces have to be evaluated. In Figure 1(a) conceptual model of the helicoidal toroidal configuration studied is illustrated. The device consists of six different parts: i) a helical toroidal permanent magnet A, ii) a curvilinear screw B, iii) a lobed ring C, iv) six rolling bearings D, vi) a permanent magnet shaped as a circular sector E, and vi) a pin F. The magnets A and B are fixed, have no relative motion. Conversely, the lobed C ring is coupled by the bearings D to B. When C is rotated around the screw B, the outer rings of the bearings roll on the lateral sides of the screw threads B. Since the inner rings of the bearings are integral to C, when C rotates around B also it moves forward or backward along the circumferential axis of B (in Figure 1 this axis is not shown). Therefore, the set C and D defines a female screw coupled to a curvilinear screw B. Consequently, also the motion of C around B toroidal helicoidal. Since the pin F is integral to C, F has the same motion C. A permanent magnet E shaped with a circular sector shape is fixed to the end of F. So, when C rotates around B, also the magnet E moves with the toroidal helical motion previously quoted. Since the screw B and the toroidal helical magnet A have the same step, if during the motion of the lobed ring C around B the magnet E rotates appropriately around the pin F, the distance between the facing surfaces of the magnets E and A does not change. The magnetization vector $\mathbf{M}$ of the magnet A is applied along the binormal unit vector relative to the barycentric helical toroidal curve of the same magnet. E has a magnetization $\mathbf{M}$ parallel to the rectilinear edges of the polarized angular sector (see the magnification in Figure 1). This $\mathbf{M}$ is equal but opposite with respect the magnetization of A. By the helical toroidal coupling between B and C, whatever is the position of C, the magnetization of A and E are always aligned towards the binormal unit vector relative to the barycentric helical toroidal curve of the magnet A. In Figure 2 a prototype of the coupling C-B is shown. The device has been manufactured with a 3D printer and allows us to obtain a helical toroidal motion of the part C. The precision of such motion can also be increased by more complicated devices [19]. In Figure 3(a) the lobed ring C is illustrated in greater detail. We note the six bearing D which can rotate as indicated by the curved arrows. The external rings of these bearings rotate while the internal rings are integral to the C body (the internal rings are fixed to C by suitable screws). In Figure 3(a), $\mathrm{W_C}$ denotes the contact points of the bearings with the three threads of the helical toroidal screw B. In order to define exactly the contact points $\mathrm{W_C}$, the transversal sections of the three threads of the screws are also lobed [see Figure 3(b)]. We can also observe that during the motion of the ring C, its centre U_m always belongs to the barycentric circumference Γ_R of the helical toroidal screw B. Moreover, whatever the position of C is, between the magnet E facing the magnet A there is always an air gap. This air gap is obtained by fixing a suitable relative position of the magnet A in relation to the helical toroidal screw B. From a mechanical point of view, the system has two degrees of freedom (DOFs): the first one defines the position of the part C in relation to the screw B, the second one fixes the position of the magnet E in relation to C [E can rotate around the axis of the pin F, see the curved arrow around the axis U_m-K_m of F in Figure 3(a)]. For example, the first DOF can be chosen as a rotation angle of the part C around the tangent *s*-*s* to the circumference Γ_R of the helical toroidal screw B atthe point U_m [see Figure 3(a)]. By imposing this rotation, the part C moves with a helical toroidal motion around the curvilinear screw B. The surface S_a of the magnet E facing the magnet A is indicated in Figure 3(a). The point K_m denotes the barycentre of this surface (a circular sector). The common rotation axis of the pin F and the magnet E belongs to S_a and passes through its barycentre K_m (see also the magnification in Figure 1). A repulsion magnetic force is applied by the magnet A to the polarized circular sector E. If we impose a value to the rotational DOF around the axis U_m-K_m, E can move only along the DOF that defines its helicoidal toroidal motion. Therefore, the repulsion force causes the motion of C together with the parts integral to it, that is, in particular, the same magnet E. The force applied by A to E depends on the value of the rotational DOF around the axis U_m-K_m that we have fixed. Consequently, for each pair of values imposed on the two DOFs previously mentioned, we obtain a certain force applied by A to E.

In this basic study, electrical coils and the relative currents and effects have not been considered yet. At the present time, evaluations of forces and torques applied by the magnet E to the magnet A by using the finite element method [20–22] have been partially tried, but the results obtained were not very reliable. Additionally, the time computation was very high and also various 3D CAD/CAE models were very difficult to manage. On the contrary, even though complex formulations are necessary, the magnetic charges method [23–30] allows a quick and accurate evaluation of the forces/moments applied

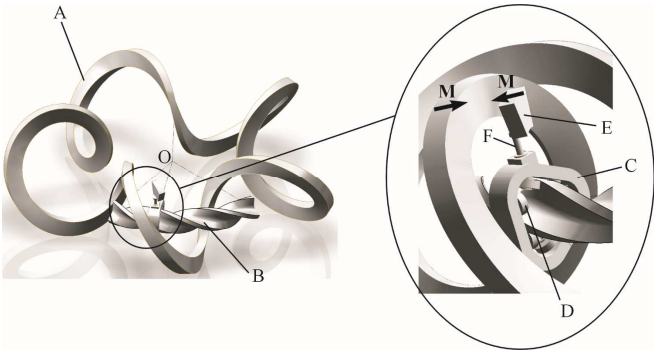

Figure 1. CAD3D model of a helical toroidal system with permanent magnets.

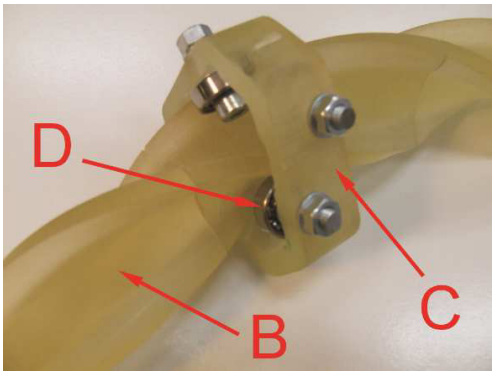

Figure 2. Curvilinear screw and lobed ring with bearings printed with a 3D printer.

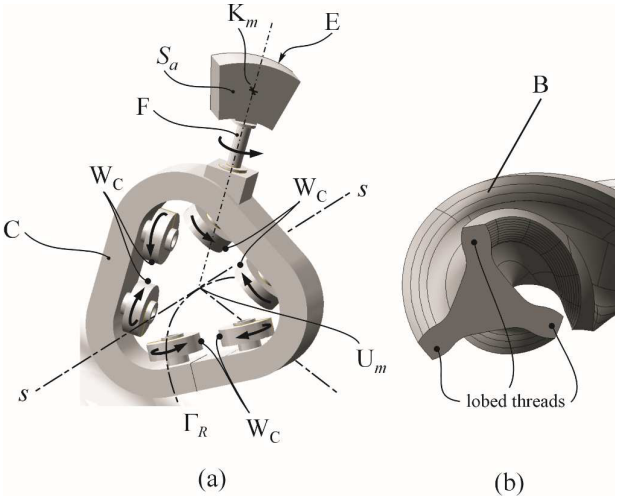

Figure 3. (a) Details of the lobed ring C, magnet E, and pin F. (b) Curvilinear lobed screw B.

to the moving permanent magnet E. In the following paragraphs we describe how the magnetic charges model has been implemented to perform the calculations and the results obtained regarding certain relative positions between the magnets A and E.

2. PHYSICAL MODELING OF THE SYSTEM FROM A QUALITATIVE POINT OF VIEW

In order to define a mathematical physical model for performing the computation of the forces and moments applied to the polarized angular sector E, it is convenient to describe the system in a qualitative way, without any mathematical detail. During the helical toroidal motion of the ring C, any point of C describes a corresponding helical toroidal path around the circular axis Γ_R of the screw B (see Figures 3 and 2). We can consider especially, a point W of the pin F axis U_m-K_m. Figure 4(a) shows the path Γ_W generated by W: it always belongs to the illustrated torus. The radius of the torus cross section is denoted by r_G. This radius is equal to the distance between the points U_m and W. The contact points W_C of the six bearings D with the three threads of the curvilinear screw B (see Figures 1–3) always belongs to the same torus surface. Therefore, we can choose r_G exactly equal to the radius of the torus to which the points W_C belong. v-v is the axis of the torus whose centre is the point O. In Figure 4(b) a sixth of the curvilinear screw B is illustrated. This part is extended from the point O_i to O_f of the relative curvilinear axis Γ_R of radius R. In this drawing the helical toroidal curve Γ_W is indicated by a dashed-dot line. It belongs to the torus previously cited and illustrated in Figure 4(a).

In Figure 4(b), only the initial and final circumferences of radius r_G of the torus have been reported (the circumferences are drawn by a dashed-dot line and their centres are the points O_i and O_f). The extremes of the path Γ_W are the points V_i and V_f that belong to the two circumferences of radius r_G. The force applied by the helical toroidal magnet A to the facing surface S_a of the polarized angular sector (magnet E) is indicated by the vector $\mathbf{F}_{\boldsymbol{Sa}}$. In this first qualitative analysis we can assume that this force is applied to the barycentre K_m of S_a. So we can see that $\mathbf{F}_{\boldsymbol{Sa}}$ generates a torque related to the point W. As a matter of fact, the contact points W_C between the bearings D and the threads of the screw B defines a constraint that causes the helical toroidal motion of the set of parts E, F, and C (see Figure 1). The distance from the application point K_m of $\mathbf{F}_{\boldsymbol{Sa}}$ and such constraint is exactly equal to the segment K_mW (W always belongs to the torus of radius r_G to which the helical toroidal paths of the contact points W_C also belong).

Therefore, also a moment $\boldsymbol{\tau}_{\boldsymbol{SaW}}$ due to $\mathbf{F}_{\boldsymbol{Sa}}$ is applied to the parts E, F, and C. Now we can consider the component $\boldsymbol{\tau}_{\boldsymbol{SaWs}}$ of $\boldsymbol{\tau}_{\boldsymbol{SaW}}$ along the tangent s-s [(see Figure 4(b)]. $\boldsymbol{\tau}_{\boldsymbol{SaWs}}$ contributes to defining a rotation of the previous parts along the rotational DOF that defines their position regarding the curvilinear screw B. In Figure 4(c) the schematized representation of the geometry that fixes the motion of the moving element E-F-C is illustrated. The computation of the previous forces and moments is based on the magnetic induction $\mathbf{B}_{\boldsymbol{Sa}}$ evaluation on the surface S_a of the generic polarized angular sector. Figure 5 shows the field $\mathbf{B}_{\boldsymbol{Sa}}$ generated by A and evaluated on S_a with the magnetic charge method. The evaluation of $\mathbf{B}_{\boldsymbol{Sa}}$ has previously been performed on all the 70 polarized sectors illustrated in the figure.The detailed procedure of the $\mathbf{B}_{\boldsymbol{Sa}}$ computation and the results only relative to the surface

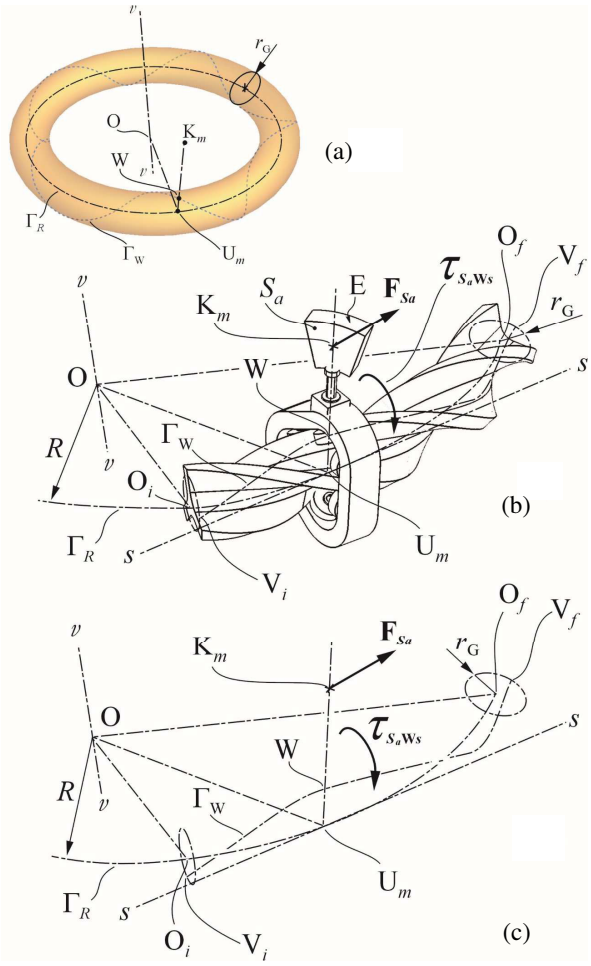

Figure 4. (a) Torus that contains the path Γ_W of the point W. (b) Force $\mathbf{F}_{\boldsymbol{Sa}}$ and moment $\boldsymbol{\tau}_{\boldsymbol{SaWs}}$ applied to the surface S_a of the magnet E. (c) Schematization of the system illustrated in (b).

S_a are illustrated in [6]. In Appendix A a short explanation of the $\mathbf{B}_{\boldsymbol{Sa}}$ computation is reported. By using a similar procedure we compute $\mathbf{B}_{\boldsymbol{Sb}}$. The position of S_a is defined by fixing 70 different values of the angular DOF around the tangent s-s of the moving element E-F-C. In order to define the total force and moment applied to the moving parts, all the previous considerations relative to the surface S_a must be suitably extended to the other surfaces of the magnet E. In the following section this aspect will be examined in detail.

3. PHYSICAL MODELING OF THE SYSTEM FROM A QUANTITATIVE POINT OF VIEW

3.1. Symbology

In relation to the complexity of the system geometry, an early complete description of the meaning of the symbols adopted is suitable. The angular polarized sector E is illustrated in Figure 6(a). We note the plane surface S_a and also the opposite one S_b that, for simplicity, has not been mentioned yet. Actually, the shape of the permanent magnet E is defined by i) two parallel plane angular sectors S_a and S_b, ii) two coaxial cylindrical surfaces of radii r_1 and r_2, and iii) two rectangular surfaces [(see Figure 6(a)]. The magnetization vector $\mathbf{M}$ of E (qualitatively indicated in Figure 1) is exactly oriented as illustrated in Figure 6(a) i.e., it is constant and perpendicular to the surfaces S_a and S_b. In relation to Figure 4(b), we can observe that during the motion of E-F-C, the point K_m (the barycentre of S_a) describes a helical toroidal curve Γ_m coaxial to Γ_W [see Figures 4 and 6(a)]. This coaxiality is true because Γ_m is obtained by rotating the helical toroidal curve Γ of an angle $\Delta\theta_m$ around the axis Z. This axis Z substitutes the axis v-v indicated in Figures 4 and 5. The curve Γ is the barycentric curve of the helical toroidal surface of the magnet A facing the surface S_a (see Figures 1 and 5).

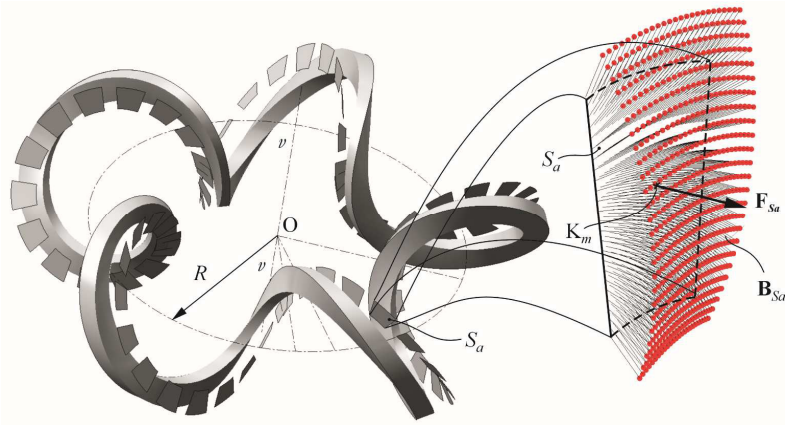

Figure 5. Semi-quantitative representation of the magnetic induction $\mathbf{B}_{\boldsymbol{Sa}}$ evaluated in 625 points of the surface S_a and corresponding force $\mathbf{F}_{\boldsymbol{Sa}}$ applied in the point K_m of S_a.

Again regarding Figure 6(a), we note that Γ belongs to another torus coaxial to the torus of radius r_G indicated in Figure 4(a). The radius of the circular transversal section of this new torus is r_m . When this radius moves with a helical toroidal motion around the circumference Γ_R, generates Γ. Figure 6(a) shows r_m whose origin is the point U that belongs to the circumference Γ_R. The other extreme point of r_m is K, which belongs to Γ. The angular position of r_m is defined by the angle $2\pi\theta_\mathbf{U}/\theta_p$ where $\theta_p = 2\pi/n$ and n is equal to the number of turns of Γ (in Figures 1 and 5 $n = 5$ coils). $\theta_\mathbf{U}$ identifies the angular position of the point U and changes from 0 to 2π rad. In this way, by fixing $n = 5$ coils, we draw the barycentric curve Γ of the surface of the magnet A facing the surface S_a. The tangent t-t indicated in Figure 6(a) to Γ in K defines the position of the corresponding tangent t_m-t_m to Γ_m in K_m: we rotate t-t around the axis Z at the previously quoted angle $\Delta\theta_m$ and obtain t_m-t_m. Therefore, as soon as the values of $\Delta\theta_m$, $\theta_\mathbf{U}$, r_m, r_1, r_2, R, the thickness b, and the semiangle φ of the polarized angular sector E are fixed, we can quantitatively define the position of E during its motion around the

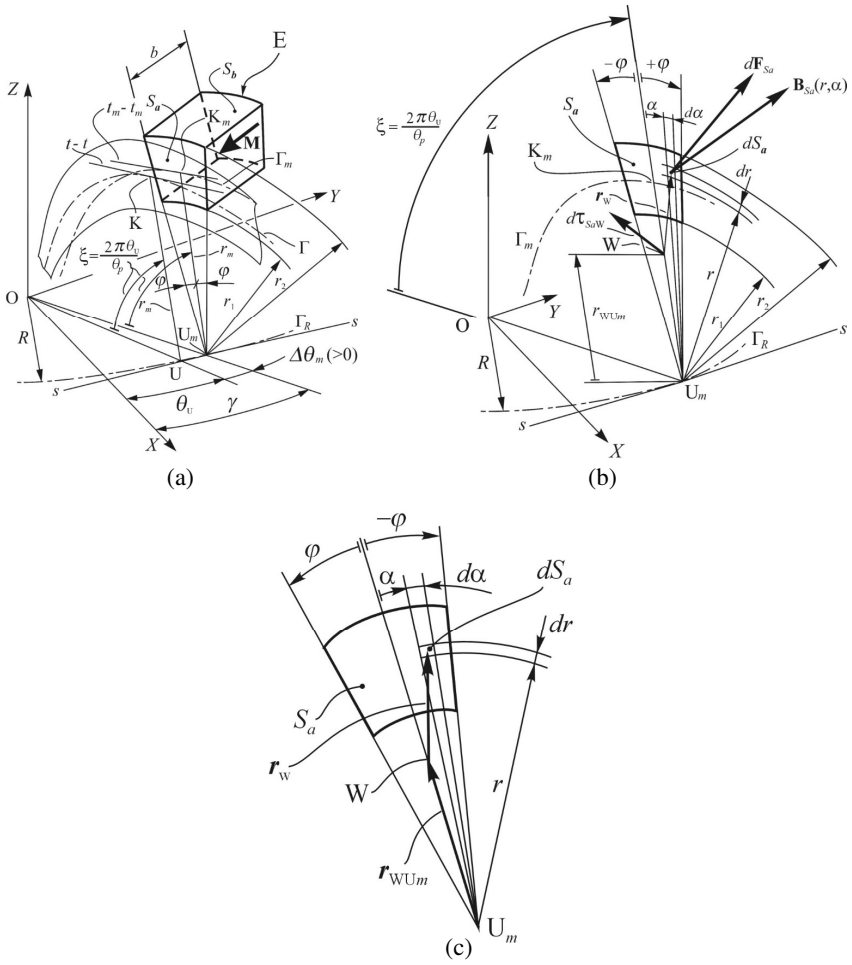

Figure 6. (a) Definition of the polarized sector geometry E. (b) Infinitesimal moment $\mathbf{d\tau_{Sa}}_{\mathbf{W}}$ and force $\mathbf{dF_{Sa}}$ applied to a point of the surface S_a. (c) Surface S_a seen along the direction of its magnetization $\mathbf{M}$.

angular screw B. In the present case study, we have fixed *a priori* the angular position of the magnet E around the axis of the pin F [see Figures 1 and 3(a)]. So, we have removed this degree of freedom by fixing the position of the tangent t_m-t_m. We can also note that t_m-t_m and the segment U_m-K_m define the angular position of the surface S_a around the same segment U_m-K_m (the axis of the pin F). Consequently, the position of the moving magnet E is defined. Finally, we observe that edges b of E are not parallel to the tangent s-s to the circumference Γ_R at the point U_m. All the symbols used in Figure 6 are tuned to those considered in [6].

3.2. Magnetostatic Model

In order to perform the computation of the forces and moments applied by the magnet A to the magnet B the magnetic charges method [23–30] has been considered. This approach integrates Maxwell equations

$$\nabla \times \mathbf{H} = 0, \tag{1}$$

$$\nabla \cdot \mathbf{B} = 0, \tag{2}$$

($\mathbf{H}$ and $\mathbf{B}$ represent the magnetic field strength and the magnetic flux density, respectively) by using the so-called volume charge density $\rho_{\mathbf{M}}(\mathbf{P})$ and surface charge density $\sigma_{\mathbf{M}}(P)$ relative to the point P of a magnet:

$$\rho_{\mathbf{M}}(\mathbf{P}) \equiv -\nabla \cdot \mathbf{M}(\mathbf{P}), \tag{3}$$

$$\sigma_{\mathbf{M}}(\mathbf{P}) \equiv \mathbf{M}(\mathbf{P}) \cdot \hat{\mathbf{n}}. \tag{4}$$

The magnetic flux densities $\mathbf{B}_{\boldsymbol{Sa}}$ and $\mathbf{B}_{\boldsymbol{Sb}}$ on the respective surfaces S_a and S_b of the moving magnet E [see Figure 6(a)] have been computed versus many values of the angle $2\pi\theta_{\mathrm{U}}/\theta_p$. For simplicity, this computation has been performed by considering only the surface charge density $\sigma_{\mathrm{M}}(\mathbf{P})$. The direction of the magnetization vector $\mathbf{M}$ of the helical toroidal magnet A that generates $\mathbf{B}_{\boldsymbol{Sa}}$ and $\mathbf{B}_{\boldsymbol{Sb}}$ was considered equal to that of the binormal unit vector related to an additional toroidal helix. This additional curve is the barycentric toroidal helix of the permanent magnet A (it is not illustrated in any figure).

3.3. Evaluation of the Forces

The computation of the forces is based on the equation [27]

$$\mathbf{F} = \int_V \rho_{\mathrm{M}} \mathbf{B}_{\mathbf{ext}} dV + \oint_S \sigma_{\mathrm{M}} \mathbf{B}_{\mathbf{ext}} dS \tag{5}$$

that has been obtained by applying the magnetic charges method [23–30]. Eq. (5) gives the force $\mathbf{F}$ applied for example to a permanent magnet immersed in an external magnetic field $\mathbf{B}_{\mathbf{ext}}$. The argument of the first integral in Eq. (5) represents the infinitesimal magnetic force applied from an external magnetic field $\mathbf{B}_{\mathbf{ext}}$ at a point $\mathbf{P}'$ of a permanent magnet whose volume charge density at $\mathbf{P}'$ is ρ_{M}. dV is the infinitesimal volume around $\mathbf{P}'$. The argument of the second integral in Eq. (5) is the infinitesimal magnetic force applied from $\mathbf{B}_{\mathbf{ext}}$ to the infinitesimal surface dS of the magnet bounding surface S. σ_{M} is the surface charge density of dS. The second integral is a surface integral evaluated on the close surface S. Regarding the simplifying hypothesis discussed in Paragraph 3.2, we evaluate the forces applied to the moving polarized magnet E by considering only the surface charge density σ_{M}. Furthermore, since the magnetization vector $\mathbf{M}$ of E is oriented towards the thickness b of the same magnet [see Figure 6(a)], only the surfaces S_a and S_b define the forces applied to E. These forces $\mathbf{F}_{\boldsymbol{Sa}}$ and $\mathbf{F}_{\boldsymbol{Sb}}$ applied to S_a and S_b, respectively, are

$$\mathbf{F}_{\boldsymbol{Sa}} = \int_{Sa} \sigma_{\mathrm{M}a}(\mathbf{P}') \mathbf{B}_{\boldsymbol{Sa}}(\mathbf{P}') dS_a, \tag{6}$$

$$\mathbf{F}_{\boldsymbol{Sb}} = \int_{Sb} \sigma_{\mathrm{M}b}(\mathbf{P}') \mathbf{B}_{\boldsymbol{Sb}}(\mathbf{P}') dS_b, \tag{7}$$

where

$$\sigma_{\mathrm{M}a}(\mathbf{P}') = \mathbf{M} \times \hat{\mathbf{n}}_a, \tag{8}$$

$$\sigma_{\mathrm{M}b}(\mathbf{P}') = \mathbf{M} \times \hat{\mathbf{n}}_b. \tag{9}$$

$\sigma_{\mathrm{M}a}(\mathbf{P}')$ and $\sigma_{\mathrm{M}b}(\mathbf{P}')$ are the surface charge densities of the surfaces S_a and S_b, respectively. $\mathbf{P}'$ is the vector that identifies the point where the surface charge density is evaluated. The starting point of this vector coincides with the origin of the absolute reference system O(X, Y, Z) [see Figure 6]. Since the magnetization $\mathbf{M}$ is parallel to the two outgoing versors $\hat{\mathbf{n}}_a$ and $\hat{\mathbf{n}}_b$ related to the corresponding surfaces S_a and S_b, we obtain

$$\sigma_{\mathrm{M}a}(\mathbf{P}') = M, \tag{10}$$

$$\sigma_{\mathrm{M}b}(\mathbf{P}') = -M. \tag{11}$$

The sign "−" in Eq. (11) indicates that the direction of $\mathbf{M}$ is opposite to that of $\hat{\mathbf{n}}_b$. M is the module of $\mathbf{M}$. We note that $\sigma_{\mathrm{M}a}(\mathbf{P}')$and $\sigma_{\mathrm{M}b}(\mathbf{P}')$ are constant at each point of S_a and S_b. The infinitesimal surface dS_a is an angular sector [see Figures 6(b) and 6(c)]. Consequently, we have

$$dS_a = r d\alpha dr. \tag{12}$$

The expression of dS_b is equal to that of dS_a, that is

$$dS_b = dS_a. \tag{13}$$

The infinitesimal forces

$$\mathbf{dF}_{\boldsymbol{Sa}} = \sigma_{\mathrm{M}a}(\mathbf{P}') \mathbf{B}_{\boldsymbol{Sa}}(\mathbf{P}') dS_a, \tag{14}$$

$$\mathbf{dF}_{\boldsymbol{Sb}} = \sigma_{\mathrm{M}b}(\mathbf{P}') \mathbf{B}_{\boldsymbol{Sb}}(\mathbf{P}') dS_b, \tag{15}$$

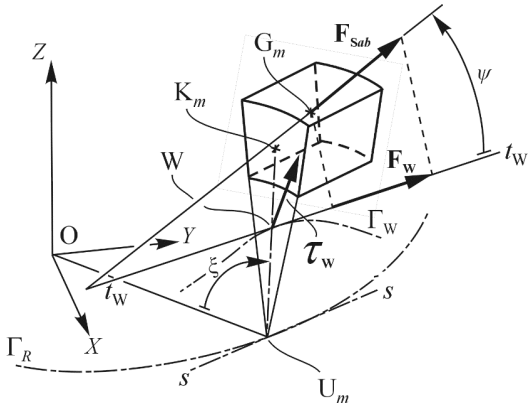

Figure 7. Force $\mathbf{F}_{\boldsymbol{Sab}}$ and moment $\boldsymbol{\tau}_{\mathbf{W}}$ applied to the polarized angular sector.

are applied to dS_a and dS_b. By integrating these forces on the whole surfaces S_a and S_b, we obtain $\mathbf{F}_{\boldsymbol{Sa}}$ and $\mathbf{F}_{\boldsymbol{Sb}}$ [see Eqs. (5) and (6)]. The resultant force $\mathbf{F}_{\boldsymbol{Sab}}$ applied to the magnet E is

$$\mathbf{F}_{\boldsymbol{Sab}} = \mathbf{F}_{\boldsymbol{Sa}} + \mathbf{F}_{\boldsymbol{Sb}}. \tag{16}$$

The force $\mathbf{F}_{\boldsymbol{Sab}}$ is illustrated in Figure 7. It is applied to the point denoted by G_m which, as an approximation, can be considered the barycentre of the magnet E. Eqs. (6) and (7) correspond to the following six scalar equations

$$F_{Sax} = M \int_{-\varphi}^{\varphi} \int_{\mathbf{r}_1}^{\mathbf{r}_2} B_{Sax}(r,\alpha,\xi) r d\alpha dr, \tag{17}$$

$$F_{Say} = M \int_{-\varphi}^{\varphi} \int_{\mathbf{r}_1}^{\mathbf{r}_2} B_{Say}(r,\alpha,\xi) r d\alpha dr, \tag{18}$$

$$F_{Saz} = M \int_{-\varphi}^{\varphi} \int_{\mathbf{r}_1}^{\mathbf{r}_2} B_{Saz}(r,\alpha,\xi) r d\alpha dr, \tag{19}$$

$$F_{Sbx} = -M \int_{-\varphi}^{\varphi} \int_{\mathbf{r}_1}^{\mathbf{r}_2} B_{Sbx}(r,\alpha,\xi) r d\alpha dr, \tag{20}$$

$$F_{Sby} = -M \int_{-\varphi}^{\varphi} \int_{\mathbf{r}_1}^{\mathbf{r}_2} B_{Sby}(r,\alpha,\xi) r d\alpha dr, \tag{21}$$

$$F_{Sbz} = -M \int_{-\varphi}^{\varphi} \int_{\mathbf{r}_1}^{\mathbf{r}_2} B_{Sbz}(r,\alpha,\xi) r d\alpha dr, \tag{22}$$

that define the moduli with the signs of the components of the forces $\mathbf{F}_{\boldsymbol{Sa}}$ and $\mathbf{F}_{\boldsymbol{Sb}}$ with reference to the system O(X, Y, Z) (see Figure 6). ξ is the angle that defines the angular position of the polarized sector E (see Figure 6):

$$\xi = \frac{2\pi\theta_{\mathbf{U}}}{\theta_p}. \tag{23}$$

Eqs. (17)–(22) are obtained by substituting Eqs. (8) and (9) in Eqs. (6) and (7), respectively. Therefore, by Eqs. (12) and (13), we obtained Eqs. (17)–(22). φ is the half angle of the plane sectors S_a and S_b.

r_1 and r_2 define the smaller and higher radii, respectively, of the same sectors (see Figure 6). To make Figure 6(b) clearer, only the surface S_a is shown [(see also Figure 6(c)]. The surface S_b is similar to S_a and it is obtained by shifting S_a from a quantity b behind S_a [see Figure 6(a)]. The quantities $B_{Sax}(r,\alpha,\xi)$, $B_{Say}(r,\alpha,\xi)$, $B_{Saz}(r,\alpha,\xi)$, $B_{Sbx}(r,\alpha,\xi)$, $B_{Sby}(r,\alpha,\xi)$, and $B_{Sbz}(r,\alpha,\xi)$ are the moduli with the signs of the components of the magnetic inductions $\mathbf{B}_{\boldsymbol{Sa}}$ and $\mathbf{B}_{\boldsymbol{Sb}}$, that is

$$\mathbf{B}_{\boldsymbol{Sa}} = \mathbf{B}_{\boldsymbol{Sa}}(B_{Sax}(r,\alpha,\xi), B_{Say}(r,\alpha,\xi), B_{Saz}(r,\alpha,\xi)), \tag{24}$$

$$\mathbf{B}_{\boldsymbol{Sb}} = \mathbf{B}_{\boldsymbol{Sb}}(B_{Sbx}(r,\alpha,\xi), B_{Sby}(r,\alpha,\xi), B_{Sbz}(r,\alpha,\xi)). \tag{25}$$

These components have been computed for each angular sector S_a and S_b versus the angle ξ.

3.4. Evaluation of the Moments

The computation of the torque applied to the polarized sector E has been performed referring to the point W [see Figures 4, 6(b), and 6(c)]. As illustrated in Section 2, $\boldsymbol{\tau_{Sa\mathrm{W}}}$ represents the moment generated from the magnetic forces applied to the surface S_a. $\boldsymbol{\tau_{Sa\mathrm{W}}}$ is obtained by integrating the infinitesimal moment

$$\mathbf{d}\boldsymbol{\tau_{Sa\mathrm{W}}} = \boldsymbol{r}_{\mathbf{W}} \times \mathbf{dF}_{\boldsymbol{Sa}}, \tag{26}$$

where $\boldsymbol{r}_{\mathbf{W}}$ is the vector that identifies the position of dS_a related to W [see Figures 6(b), (c)]. By substituting Eqs. (10) and (12) in Eq. (14), we obtain a new expression of $\mathbf{dF}_{\boldsymbol{Sa}}$. By putting this new $\mathbf{dF}_{\boldsymbol{Sa}}$ expression in Eq. (26) we achieve

$$\mathbf{d}\boldsymbol{\tau_{Sa\mathrm{W}}} = \boldsymbol{r}_{\mathbf{W}} \times \mathbf{B}_{\boldsymbol{Sa}}(r,\alpha,\xi) M r d\alpha dr. \tag{27}$$

Therefore,

$$\boldsymbol{\tau_{Sa\mathrm{W}}} = \int_{-\varphi}^{\varphi} \int_{\mathbf{r}_1}^{\mathbf{r}_2} \boldsymbol{r}_{\mathbf{W}} \times \mathbf{B}_{\boldsymbol{Sa}}(r,\alpha,\xi) M r d\alpha dr. \tag{28}$$

The computation of $\boldsymbol{\tau_{Sa\mathrm{W}}}$ by Eq. (28) is performed by evaluating its three components $\boldsymbol{\tau_{Sa\mathrm{W}x}}$, $\boldsymbol{\tau_{Sa\mathrm{W}y}}$, and $\boldsymbol{\tau_{Sa\mathrm{W}z}}$ connected to the reference system O(X, Y, Z). The moduli with the signs of the previous three components are:

$$\tau_{Sa\mathrm{W}x} = M \int_{-\varphi}^{\varphi} \int_{r_1}^{r_2} [r_{\mathrm{W}y} B_{Saz}(r,\alpha,\xi) - r_{\mathrm{W}z} B_{Say}(r,\alpha,\xi)] r d\alpha dr, \tag{29}$$

$$\tau_{Sa\mathrm{W}y} = M \int_{-\varphi}^{\varphi} \int_{r_1}^{r_2} [r_{\mathrm{W}z} B_{Sax}(r,\alpha,\xi) - r_{\mathrm{W}x} B_{Saz}(r,\alpha,\xi)] r d\alpha dr, \tag{30}$$

$$\tau_{Sa\mathrm{W}z} = M \int_{-\varphi}^{\varphi} \int_{r_1}^{r_2} [r_{\mathrm{W}x} B_{Say}(r,\alpha,\xi) - r_{\mathrm{W}y} B_{Say}(r,\alpha,\xi)] r d\alpha dr. \tag{31}$$

$r_{\mathrm{W}x}$, $r_{\mathrm{W}y}$, and $r_{\mathrm{W}z}$ are the moduli with the signs of the components of the vector r_{W} [always referring to the same system O(X, Y, Z)]. Similarly, we obtain the corresponding moment $\boldsymbol{\tau_{Sb\mathrm{W}}}$ caused by the other surface S_b:

$$d\boldsymbol{\tau_{Sb\mathrm{W}}} = \boldsymbol{r}'_{\mathbf{W}} \times \mathbf{dF}_{\boldsymbol{Sb}}, \tag{32}$$

$$d\boldsymbol{\tau_{Sb\mathrm{W}}} = -\boldsymbol{r}'_{\mathbf{W}} \times \mathbf{B}_{\boldsymbol{Sb}}(r,\alpha,\xi) M r d\alpha dr, \tag{33}$$

$$\boldsymbol{\tau_{Sb\mathrm{W}}} = -\int_{-\varphi}^{\varphi} \int_{\boldsymbol{r}_1}^{\boldsymbol{r}_2} \boldsymbol{r}'_{\mathbf{W}} \times \mathbf{B}_{\boldsymbol{Sb}}(r,\alpha,\xi) M r d\alpha dr, \tag{34}$$

$$\tau_{Sb\mathrm{W}}x = -M\int_{-\varphi}^{\varphi}\int_{r_1}^{r_2}[r'_{\mathrm{W}y}B_{Sbz}(r,\alpha,\xi) - r'_{\mathrm{W}z}B_{Sby}(r,\alpha,\xi)]rd\alpha dr, \tag{35}$$

$$\tau_{Sb\mathrm{W}y} = -M\int_{-\varphi}^{\varphi}\int_{r_1}^{r_2}[r'_{\mathrm{W}z}B_{Sbx}(r,\alpha,\xi) - r'_{\mathrm{W}x}B_{Sbz}(r,\alpha,\xi)]rd\alpha dr, \tag{36}$$

$$\tau_{Sb\mathrm{W}z} = -M\int_{-\varphi}^{\varphi}\int_{r_1}^{r_2}[r'_{\mathrm{W}x}B_{Sby}(r,\alpha,\xi) - r'_{\mathrm{W}y}B_{Sby}(r,\alpha,\xi)]rd\alpha dr, \tag{37}$$

$\boldsymbol{r'_{\mathrm{W}}}$ is the vector that identifies the infinitesimal surface dS_b related the point W. $r'_{\mathrm{W}x}$, $r'_{\mathrm{W}y}$, and $r'_{\mathrm{W}z}$ are the moduli with the signs of the corresponding components, in the reference system O(X, Y, Z). By observing Figures 6(a) and 6(b), we infer that

$$\boldsymbol{r'_{\mathrm{W}}} = \boldsymbol{r_{\mathrm{W}}} + \mathbf{b}, \tag{38}$$

where $\mathbf{b}$ is the vector that identifies the position of the surface dS_b starting from the corresponding surface dS_a [to make Figure 6(b) clearer, the vectors $\mathbf{b}$ and $\boldsymbol{r'_{\mathrm{W}}}$ have not been drawn]. $\mathbf{b}$ is parallel to the four rectilinear edges of the polarized sector E and its module is equal to b [see the thickness of E indicated in Figure 6(a)]. $\boldsymbol{r_{\mathrm{W}}}$ and $\boldsymbol{r'_{\mathrm{W}}}$ are functions of r, α, ξ, and $\boldsymbol{r_{\mathrm{W}U_m}}(\xi)$, the vector that identifies the point W from the point U_m [see Figure 6(b)]. The evaluation of $\boldsymbol{r_{\mathrm{W}}}$ and $\boldsymbol{r'_{\mathrm{W}}}$ is explained in Appendix B. Finally, the resultant moment applied to the moving magnet E and, consequently, to F (pin) and C (lobed ring) related tothe point W [see Figures 1–3, 4(b)] is equal to

$$\boldsymbol{\tau}_{\mathrm{W}} = \boldsymbol{\tau_{Sa\mathrm{W}}} + \boldsymbol{\tau_{Sb\mathrm{W}}}. \tag{39}$$

4. EVALUATION OF THE FORCE AND WORK ALONG THE HELICAL TOROIDAL PATH Γ_{W}

The toroidal helix Γ_{W} is the path that the point W of the F pin axis describes when the set of parts E-F-C rotates around the curvilinear screw A (see Figures 1 and 4). The force $\mathbf{F_{Sab}}$ and the torque $\boldsymbol{\tau}_{\mathbf{W}}$ move the previous parts set along Γ_{W}. In consideration of possible applications, the knowledge of how the work generated from $\mathbf{F_{Sab}}$ and $\boldsymbol{\tau}_{\mathbf{W}}$ changes versus the rotation ξ of the whole set E-F-C around the tangent *s*-*s* [see Figure 6(a) and (23)] is important. As mentioned in the previous section, we impose *a priori* position of the polarized sector E facing the helical toroidal magnet A. In the case study we fix this position in such a way that the surface S_a always belongs to the tangent t_m-t_m of the toroidal helix Γ_m [see Figures 6(a) and 6(b)]. The tangent at point K_m belongs to S_a, whatever the value of ξ is. Connected to this hypothesis, by the previous formulae it is possible to evaluate $\mathbf{F_{Sab}}$, $\boldsymbol{\tau}_{\mathbf{W}}$, and the corresponding work versus ξ. We note that the fixed position around the pin F axis U_m-K_m of the polarized sector E, is certainly not the real position of E: to define the true position it is necessary to find the equilibrium condition of E subject to the magnetic forces around U_m-K_m. Nevertheless, we leave this study for further developments. Now, considering the configuration of the system defined by the fixed position of E just illustrated, we will evaluate the work generated by the force $\mathbf{F_{Sab}}$ and the torque $\boldsymbol{\tau}_{\mathbf{W}}$ that move the same magnet E around the curvilinear screw A. The following computation procedure can be easily modified as soon as the real equilibrium position of E around the axis U_m-K_m versus ξ is known.

4.1. Evaluation of the Force $\mathbf{F_W}$ along Γ_{W}

The force $\mathbf{F_{Sab}}$ and the torque $\boldsymbol{\tau}_{\mathbf{W}}$ applied to the polarized sector E generate a work. In order to evaluate this work it is advantageous to compute the component $\mathbf{F_W}$ of $\mathbf{F_{Sab}}$ [see (16)] along the tangent t_{W}-t_{W} to Γ_{W} at the point W (see Figure 7). This force $\mathbf{F_W}$, together with the moment $\boldsymbol{\tau}_{\mathbf{W}}$ [see (39)], pushes the set of parts E-F-C and causes its helical toroidal motion around the curvilinear screw B (see Figure 1). We compute $\mathbf{F_W}$ versus ξ by the following equation

$$\mathbf{F_W}(\xi) = \mathbf{F_{Sab}}(\xi)\cos\psi(\xi), \tag{40}$$

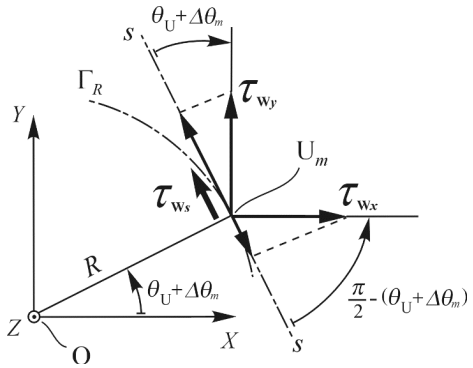

Figure 8. Evaluation of the moment component $\boldsymbol{\tau_{Ws}}$ along the tangent s-s.

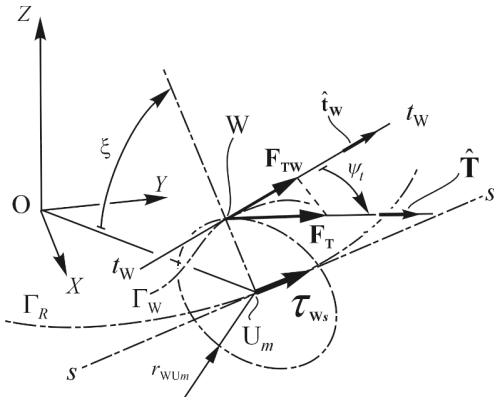

Figure 9. Evaluation of the force component $\mathbf{F_{TW}}$ along the tangent t_W-t_W to the toroidal helix Γ_W.

where $\psi(\xi)$ is the angle between $\mathbf{F_{Sab}}$ and the tangent t_W-t_W (see Figure 7). The evaluation of ψ versus ξ is illustrated in Appendix D.

4.2. Evaluation of the Force $\mathbf{F_{TW}}$ Along Γ_W

The modulus with sign τ_{Ws} of the component $\boldsymbol{\tau_{Ws}}$ of $\boldsymbol{\tau_W}$ along the tangent s-s to the circumference Γ_R in U_m (see Figure 8) is

$$\tau_{Ws} = \tau_{Wy}\cos(\theta_U + \Delta\theta_m) - \tau_{Wx}\sin(\theta_U + \Delta\theta_m), \tag{41}$$

where τ_{W_x} and τ_{W_y} are the moduli with the signs of the components of τ_W along the axes X and Y, respectively. The component along the axis Z of $\boldsymbol{\tau_W}$ is always perpendicular to s-s, therefore it can not give any contribution to $\boldsymbol{\tau_{Ws}}$ and τ_{Ws}. $\boldsymbol{\tau_{Ws}}$ tends to rotate the set of parts E-F-C along the degree of freedom ξ, which is around the tangent s-s. Consequently, the effect of $\boldsymbol{\tau_{Ws}}$ is that of a force $\mathbf{F_T}$ multiplied by the lever arm $\boldsymbol{r_{WUm}}$ that identifies the point W. This $\mathbf{F_T}$ i) is applied in W, ii) is always perpendicular to $\boldsymbol{r_{WUm}}$, and iii) always belongs to the plane on which ξ is defined (see Figure 9). So, we have

$$\mathbf{F_T} = \frac{\boldsymbol{\tau_{Ws}}}{|\boldsymbol{r_{WUm}}|}, \tag{42}$$

where $|\boldsymbol{r_{WUm}}|$ is the modulus of $\boldsymbol{r_{WUm}}$. The component $\mathbf{F_{TW}}$ of $\mathbf{F_T}$ along the tangent t_W-t_W to Γ_W at the point W contributes to push the parts set E-F-C along the same tangent t_W-t_W. Denoted by $\psi_t(\xi)$ the angle between the direction of $\mathbf{F_T}$ and t_W-t_W (see Figure 9), we obtain

$$\mathbf{F_{TW}}(\xi) = \mathbf{F_T}(\xi)\cos\psi_t(\xi). \tag{43}$$

The evaluation of ψ_t versus ξ is illustrated in Appendix C.

4.3. Evaluation of the Total Force $\mathbf{F_{Wtot}}$ along Γ_W

The total force $\mathbf{F_{Wtot}}$ that pushes the parts E-F-C along the tangent t_W-t_W and causes the helical toroidal motion of the same around the toroidal helicoidal screw B (see Figure 1) is equal to the sum of $\mathbf{F_W}$ and $\mathbf{F_{TW}}$:

$$\mathbf{F_{Wtot}}(\xi) = \mathbf{F_W}(\xi) + \mathbf{F_{TW}}(\xi). \tag{44}$$

All the forces in Eq. (44) depend on the angle ξ. Related to the ξ value, $\mathbf{F_W}$ and $\mathbf{F_{TW}}$ can have the same or opposite directions. The force $\mathbf{F_{Wtot}}$ can be advantageously used to compute the work developed from the magnetic forces applied from the magnet A to the magnet E versus ξ. In the following section, the evaluation of this work is performed.

5. EVALUATION OF THE WORKS DEVELOPED BY THE MAGNETIC FORCES

The knowledge of the works generated by the magnetic forces is very important to the evaluation of the efficiency of an electric machine. In the case study, we can limit ourselves to evaluate the works associated with the forces $\mathbf{F_W}$, $\mathbf{F_{TW}}$, and, overall, $\mathbf{F_{Wtot}}$ versus ξ. The procedure to compute these works represents a basic step in relation to other more complete evaluations that will have to be performed when electric currents and coils are considered. The infinitesimal works generated by $\mathbf{F_W}$, $\mathbf{F_{TW}}$, and $\mathbf{F_{Wtot}}$ are

$$dL_{\mathrm{W}} = \mathbf{F_W} \cdot \mathbf{d\Gamma_W}, \tag{45}$$

$$dL_{\mathrm{TW}} = \mathbf{F_{TW}} \cdot \mathbf{d\Gamma_W}, \tag{46}$$

$$dL_{\mathrm{Wtot}} = \mathbf{F_{Wtot}} \cdot \mathbf{d\Gamma_W}, \tag{47}$$

respectively. $\mathbf{d\Gamma_W}$ is the infinitesimal displacement vector of the point W belonging to the toroidal helix Γ_{W}. By denoting F_{W}, F_{TW}, and F_{Wtot} the moduli with the signs of the forces $\mathbf{F_W}$, $\mathbf{F_{TW}}$, and $\mathbf{F_{Wtot}}$, respectively, the previous works can be evaluated by the following expressions

$$dL_{\mathrm{W}} = F_{\mathrm{W}} d\Gamma_{\mathrm{W}}, \tag{48}$$

$$dL_{\mathrm{TW}} = F_{\mathrm{TW}} d\Gamma_{\mathrm{W}}, \tag{49}$$

$$dL_{\mathrm{Wtot}} = F_{\mathrm{Wtot}} d\Gamma_{\mathrm{W}}, \tag{50}$$

The signs of F_{W}, F_{TW}, and F_{Wtot} define the direction of the corresponding forces. $d\Gamma_{\mathrm{W}}$ is the modulus of $\mathbf{d\Gamma_W}$:

$$d\Gamma_{\mathrm{W}} = \sqrt{x'_{\mathrm{W}}(\theta_{\mathrm{U}})^2 + y'_{\mathrm{W}}(\theta_{\mathrm{U}})^2 + z'_{\mathrm{W}}(\theta_{\mathrm{U}})^2}\, d\theta_{\mathrm{U}}. \tag{51}$$

$x'_{\mathrm{W}}(\theta_{\mathrm{U}})$, $y'_{\mathrm{W}}(\theta_{\mathrm{U}})$, and $z'_{\mathrm{W}}(\theta_{\mathrm{U}})$ are the derivatives with respect to θ_{U} of the parametric equations $x_{\mathrm{W}}(\theta_{\mathrm{U}})$, $y_{\mathrm{W}}(\theta_{\mathrm{U}})$, and $z_{\mathrm{W}}(\theta_{\mathrm{U}})$ of Γ_{W}:

$$x_{\mathrm{W}}(\theta_{\mathrm{U}}) = (R - |\boldsymbol{r}_{\mathbf{WU}\boldsymbol{m}}| \cos\xi) \cos(\theta_{\mathrm{U}} + \Delta\theta_m), \tag{52}$$

$$y_{\mathrm{W}}(\theta_{\mathrm{U}}) = (R - |\boldsymbol{r}_{\mathbf{WU}\boldsymbol{m}}| \cos\xi) \sin(\theta_{\mathrm{U}} + \Delta\theta_m), \tag{53}$$

$$z_{\mathrm{W}}(\theta_{\mathrm{U}}) = |\boldsymbol{r}_{\mathbf{WU}\boldsymbol{m}}| \sin\xi. \tag{54}$$

ξ is furnished by Eq. (23). Therefore, we can compute the works developed by the forces $\mathbf{F_W}$, $\mathbf{F_{TW}}$, and $\mathbf{F_{Wtot}}$. By substituting Eqs. (23) and (52)–(54) in Eqs. (48)–(50), referring to $0 \le \xi \le 2\pi$, is $0 \le \theta_{\mathrm{U}} \le \theta_p$ [see Eq. (23)], we obtain:

$$L_{\mathrm{W}} = \int_0^{\theta_p} F_{\mathrm{W}} \left(\frac{2\pi\theta_{\mathrm{U}}}{\theta_p}\right) \sqrt{x'_{\mathrm{W}}(\theta_{\mathrm{U}})^2 + y'_{\mathrm{W}}(\theta_{\mathrm{U}})^2 + z'_{\mathrm{W}}(\theta_{\mathrm{U}})^2}\, d\theta_{\mathrm{U}}, \tag{55}$$

$$L_{\mathrm{TW}} = \int_0^{\theta_p} F_{\mathrm{TW}} \left(\frac{2\pi\theta_{\mathrm{U}}}{\theta_p}\right) \sqrt{x'_{\mathrm{W}}(\theta_{\mathrm{U}})^2 + y'_{\mathrm{W}}(\theta_{\mathrm{U}})^2 + z'_{\mathrm{W}}(\theta_{\mathrm{U}})^2}\, d\theta_{\mathrm{U}}, \tag{56}$$

$$L_{\mathrm{Wtot}} = \int_0^{\theta_p} F_{\mathrm{Wtot}} \left(\frac{2\pi\theta_{\mathrm{U}}}{\theta_p}\right) \sqrt{x'_{\mathrm{W}}(\theta_{\mathrm{U}})^2 + y'_{\mathrm{W}}(\theta_{\mathrm{U}})^2 + z'_{\mathrm{W}}(\theta_{\mathrm{U}})^2}\, d\theta_{\mathrm{U}}. \tag{57}$$

The total work L_{Wtot} relative to a complete rotation around the tangent s-s of the parts set E-F-C [see Figure 3(a)] is also equal to

$$L_{\mathrm{Wtot}} = L_{\mathrm{TW}} + L_{\mathrm{W}}. \tag{58}$$

6. NUMERICAL EVALUATIONS AND RESULTS

The numerical evaluations have been performed as follows: i) computing of the magnetic induction generated by the helical toroidal magnet A in a finite number of points belonging to the surfaces S_a and S_b [see Figures 1 and 6(a)] versus a finite number of ξ values, ii) defining of the response surfaces to compute the magnetic induction at any point of S_a and S_b, iii) evaluation of moments and forces applied to the polarized angular sector E, and iv) computation of the works developed by the previous forces and moments related to a complete rotation of E around the curvilinear screw B.

6.1. Evaluation of the Magnetic Induction at a Finite Number of Points

The magnetic inductions $\mathbf{B}_{\boldsymbol{Sa}}(\mathbf{P}')$ and $\mathbf{B}_{\boldsymbol{Sb}}(\mathbf{P}')$ have been computed with the magnetic charges method [23–30] as illustrated in Section 3. The choice of the points was performed following the procedure described in [6]. 625 points of each surface S_a and S_b were fixed. These surfaces have been positioned by fixing 14 values of ξ, which correspond to 14 values of $\theta_{\mathbf{U}}$ [see Eq. (23)]. Such values have been computed by Eq. (28) indicated in [6] (see also Table 2 in [6]). All the dimensions of the system are those considered in [6]. The only difference relating to the dimensions of the previous study [6] is the parameter b. For the reader's convenience, the main dimension and parameter values of the device studied are reported in Table 1. In the present study b defines the distance between S_a and S_b [see Figure 6(a)]. In [6], only the surface S_a was considered. On the contrary, to define the magnet E (in the present study) also the surface S_b has been fixed. The value of b has been put equal to 30 mm. With reference to Table 1, we can see that the value of θ_p has been put equal to 72 degrees. This value was fixed connected to the integration domains for the computation of the works defined by Eqs. (55)–(57). Such evaluations refer to a complete rotation of the whole set E-F-C around the tangent *s-s* [see Figures 1, 3(a), and 6(a)]. Nevertheless, also the set of the 14 positions of the sectors S_a and S_b where $\mathbf{B}_{\boldsymbol{Sa}}(\mathbf{P}')$ and $\mathbf{B}_{\boldsymbol{Sb}}(\mathbf{P}')$ have been computed at 625 points/sector, is defined by θ_{U} and its highest value is equal to 70.2 degrees [6]. So, for computation convenience, the evaluation of $\mathbf{B}_{\boldsymbol{Sa}}(\mathbf{P}')$ and $\mathbf{B}_{\boldsymbol{Sb}}(\mathbf{P}')$ corresponding to the 14th position of the two sectors S_a and S_b has been performed by fixing $\theta_{\mathrm{U}} = 70.2$ degrees. The different value of 72 degrees has been suitably fixed connected to the following interpolation of the magnetic inductions versus the angle ξ that changes from 0 to 360 degrees. By considering Eq. (23), we note that when $\xi = 360$ degrees, $\theta_{\mathbf{U}}$ is equal to 72 degrees. The magnetic flux densities $\mathbf{B}_{\boldsymbol{Sa}}(\mathbf{P}')$ and $\mathbf{B}_{\boldsymbol{Sb}}(\mathbf{P}')$ have been evaluated by fixing the module of the magnetization vector

Table 1. Main dimensions and parameters of the device studied.

$\lvert\mathbf{M}\rvert = 4.3 \times 10^5$ A/m			
R (mm)	r_1 (mm)	r_2 (mm)	b (mm)
220.0	67.5	97.5	30.0
$0 \leq \xi \leq 2\pi$ rad			
$0 \leq \theta_{\mathbf{U}} \leq \theta_p, \theta_p = \frac{2\pi}{5}$ rad (= 72 degrees)			
$\Delta\theta_m = 4 \times \frac{\pi}{180}$ rad (= 4 degrees)			
$\varphi = 10 \times \frac{\pi}{180}$ rad (= 10 degrees)			

Table 2. Value of the module $|\boldsymbol{r}_{\mathbf{WU}m}|$.

$\lvert\boldsymbol{r}_{\mathbf{WU}m1}\rvert$	$\lvert\boldsymbol{r}_{\mathbf{WU}m2}\rvert$	$\lvert\boldsymbol{r}_{\mathbf{WU}m3}\rvert$	$\lvert\boldsymbol{r}_{\mathbf{WU}m4}\rvert$	$\lvert\boldsymbol{r}_{\mathbf{WU}m5}\rvert$
6.75	13.50	20.25	27.00	33.75
$\lvert\boldsymbol{r}_{\mathbf{WU}m6}\rvert$	$\lvert\boldsymbol{r}_{\mathbf{WU}m7}\rvert$	$\lvert\boldsymbol{r}_{\mathbf{WU}m8}\rvert$	$\lvert\boldsymbol{r}_{\mathbf{WU}m9}\rvert$	$\lvert\boldsymbol{r}_{\mathbf{WU}m10}\rvert$
40.50	47.25	54.00	60.75	67.50
(mm)				

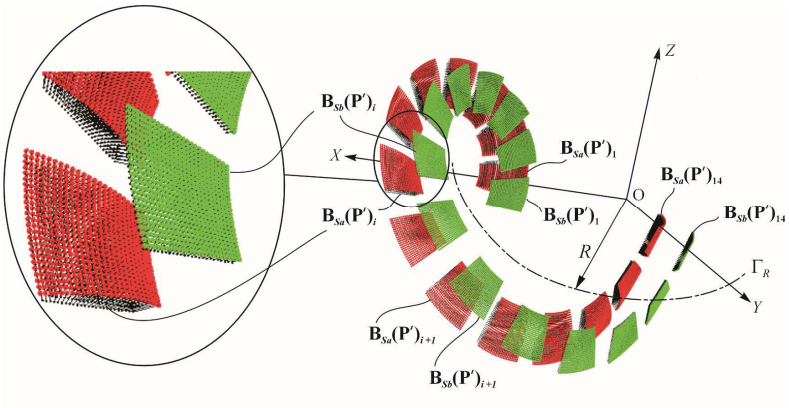

Figure 10. Magnetic flux densities evaluated on the surfaces S_a and S_b.

M indicated in Table 1. In Figure 10 a semi-quantitative representation of $\mathbf{B}_{\boldsymbol{Sa}}(\mathbf{P}')$ and $\mathbf{B}_{\boldsymbol{Sb}}(\mathbf{P}')$ is illustrated. This figure shows 625 magnetic induction vectors for each surface S_a and S_b. 14 pairs of surfaces and $2 \times 625 \times 14 = 2500$ vectors have been shown. Each pair of surfaces S_a and S_b defines a position of the polarized sector E during its helicoidal toroidal motion around the curvilinear screw B. The length of the previous vectors is suitably scaled versus their moduli. We note that the order of magnitude of the $\mathbf{B}_{\boldsymbol{Sb}}(\mathbf{P}')$ moduli can be more than ten times lower than that of $\mathbf{B}_{\boldsymbol{Sa}}(\mathbf{P}')$. $\mathbf{B}_{\boldsymbol{Sa}}(\mathbf{P}')$ has already been computed in [6]. The maximum module value of the magnetic flux density $\mathbf{B}_{\boldsymbol{Sa}}(\mathbf{P}')$ is equal to 0.1805 Tesla [6].

6.2. Response Surfaces

In order to perform the computation of the integrals in Eqs. (17)–(22), (29)–(31), and (35)–(37), the moduli with the signs $B_{Sax}(r,\alpha,\xi)$, $B_{Say}(r,\alpha,\xi)$, $B_{Saz}(r,\alpha,\xi)$, $B_{Sbx}(r,\alpha,\xi)$, $B_{Sby}(r,\alpha,\xi)$, and $B_{Sbz}(r,\alpha,\xi)$ of the components of the magnetic inductions $\mathbf{B}_{\boldsymbol{Sa}}$ and $\mathbf{B}_{\boldsymbol{Sb}}$ have to be known for each value of r, α, and ξ in the integration domain. Therefore, the previous moduli have to be continuous functions of r and α (ξ is fixed because it defines the angular position of S_a and S_b). This continuity can be obtained by using the response surfaces that interpolate the discrete values of the magnetic inductions previously evaluated at 625 points/sector S_a and S_b. In this way, we achieve a numerically continuous function for each module with its sign. Figure 11 shows an example of surface response relative to the evaluation of the module with the sign $B_{Sax}(r,\alpha,\xi)$ with $r_1 \le r \le r_2$, $-\varphi \le \alpha \le +\varphi$, and $\xi = 0$ degrees [see $\mathbf{B}_{\boldsymbol{Sa}}(\mathbf{P}')_1$ in Figure 10]. In Figure 11 $B_{Sax}(r,\alpha,\xi)$ has been denoted by $B_{Sax}(r,\alpha)_1$.

6.3. Forces and Moments Applied to the Moving Set E-F-C

The evaluation of the total force $\mathbf{F}_{\mathbf{Wtot}}$ that pushes the parts E-F-C along the tangent t_{W}-t_{W} has been performed by using Eqs. (17)–(22), (29)–(31), and (39)–(44). This force was computed relating to the fourteen positions of S_a and S_b illustrated in Figure 10. Moreover, a further position of the surfaces pair S_a and S_b has been added by fixing $\xi = 360$ degrees. The modulus with sign F_{Wtot} of $\mathbf{F}_{\mathbf{Wtot}}$ relative to this 15th position and that computed when $\xi = 0$ degrees is the same (S_a and S_b have the 1st position indicated in Figure 10). So, the magnetic field generated by the toroidal helicoidal magnet A has an axial symmetry [6] that also implies the corresponding axial symmetry of the forces generated by the same field on the sectors S_a and S_b positioned as previously described. Therefore, fifteen values of F_{Wtot} are available. The values of F_{Wtot} relative to $\xi = 0$ and 360 degrees are equal. By interpolating this 15 values with a spline curve we obtain the continuous function $F_{\mathrm{Wtot}}(\xi)$ with $0 \le \xi \le 360$ degrees. This function remains the same even when the parts E-F-C describe a complete angular rotation and start the following one. Since the toroidal helicolidal magnet A has five coils (see Figure 1), $F_{\mathrm{Wtot}}(\xi)$ represents a periodic function that repeats itself five times.

Consequently, whatever the position around the circumference Γ_R of the same set is, we obtain the force applied to the set E-F-C. In addition, we can see that $F_{\mathrm{Wtot}}(\xi)$ also depends on $|\boldsymbol{r}_{\mathbf{WU}\boldsymbol{m}}|$,

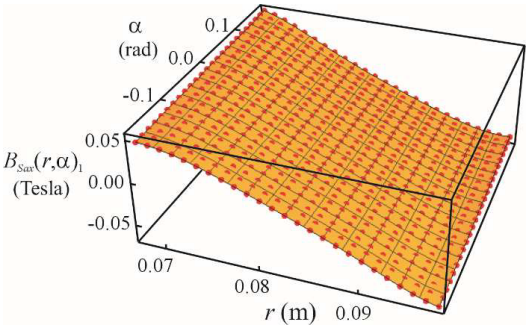

Figure 11. Surface response relative to 625 points of $\mathbf{B_{Sa}}(\mathbf{P'})$ to compute $B_{Sax}(r, \alpha, \xi)$ (case related to $\xi = 0$ degrees, see Figure 6).

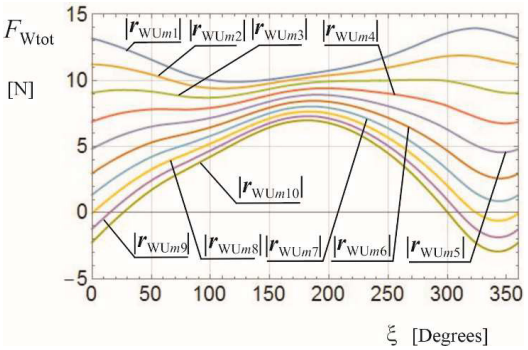

Figure 12. Total force applied to the moving set E-F-C along the tangent t_W-t_W versus ξ and $|\boldsymbol{r}_{\mathbf{WU}m}|$.

the modulus of the vector $\boldsymbol{r}_{\mathbf{WU}m}$ [see Figure 6(b), Eqs. (34)–(37), Appendix B and Section 4]. By changing the value of $|\boldsymbol{r}_{\mathbf{WU}m}|$, we achieve different curves $F_{\mathrm{Wtot}}(\xi, |\boldsymbol{r}_{\mathbf{WU}m}|)$. Figure 12 shows the curves $F_{\mathrm{Wtot}}(\xi, |\boldsymbol{r}_{\mathbf{WU}mi}|)$ related to ten different $|\boldsymbol{r}_{\mathbf{WU}mi}|$ $(i = 1, 2, \ldots 10)$. Table 2 reports the values of $|\boldsymbol{r}_{\mathbf{WU}mi}|$ considered. They have been obtained by the following relation

$$|\boldsymbol{r}_{\mathbf{WU}mi}| = i \times \frac{\boldsymbol{r}_1}{10}, \tag{59}$$

where $(i = 1, 2, \ldots 10)$. We note that in general, F_{Wtot} always has the same direction along the tangent t_W-t_W. Only when the axis of the pin F is more or less horizontal (ξ is close to 0 or 360 degrees), the F_{Wtot} direction changes (F_{Wtot} has negative values).

The computation of the torque applied to the set of the parts E-F-C has been performed by using the same numerical approach developed to compute F_{Wtot}. Therefore, the modulus with the sign $\tau_{\mathrm{W}s}$ [see Eq. (41)] of the moment $\boldsymbol{\tau}_{\mathbf{W}s}$ has been evaluated versus ξ and the same ten values of $|\boldsymbol{r}_{\mathbf{WU}mi}|$ previously fixed. Figure 13 shows the results obtained. By observing the curves reported in such figure, we note that also $\boldsymbol{\tau}_{\mathbf{W}s}$ changes its direction when ξ is close to 0 or 360 degrees. Moreover, $\tau_{\mathrm{W}s}$ correctly decreases when W tends to K_m, that is when $|\boldsymbol{r}_{\mathbf{WU}m}|$ increases and the corresponding moduli $|\mathbf{r}_{\mathbf{W}}|$ and $|\boldsymbol{r}'_{\mathbf{W}}|$ decrease [see Figure 6(b), Eqs. (B2), (26), (32), (38) and the trends of $\tau_{\mathrm{W}s}(\xi, |\boldsymbol{r}_{\mathbf{WU}m}|)$].

6.4. Evaluation of the Works

The works L_{W}, L_{TW}, and L_{Wtot} developed by the forces $\mathbf{F_W}$, $\mathbf{F_{TW}}$, and $\mathbf{F_{Wtot}}$, respectively [see Eqs. (40), (43), and (44)] have been numerically computed by solving the integrals indicated in Eqs. (55)–(57). Ten evaluations of the tern L_{W}, L_{TW}, and L_{Wtot} were performed. Each evaluation corresponded to the ten values of $|\boldsymbol{r}_{\mathbf{WU}m}|$ reported in Table 2. The corresponding ten values of each work computed have been interpolated by a spline function versus $|\boldsymbol{r}_{\mathbf{WU}m1}| \leq |\boldsymbol{r}_{\mathbf{WU}m}| \leq |\boldsymbol{r}_{\mathbf{WU}m10}|$. In this way the three functions $L_{\mathrm{W}}(|\boldsymbol{r}_{\mathbf{WU}m}|)$, $L_{\mathrm{TW}}(|\boldsymbol{r}_{\mathbf{WU}m}|)$, and $L_{\mathrm{Wtot}}(|\boldsymbol{r}_{\mathbf{WU}m}|)$ reported in Figure 14 were achieved. We note that these works are relative to a complete rotation of the parts set E-F-C around the curvilinear screw A (see Figures 1 and 4). Connected to the axial symmetry of the particular magnetic field of this device [6], L_{W}, L_{TW}, and L_{Wtot} are generated to each subsequent complete rotation of the parts E-F-C around the screw A. Therefore, the principle of energy conservation should not be outwardly satisfied. However, we must observe that i) we have fixed *a priori* the angular positions of the polarized sector E facing the magnet A and ii) the effect of the volume charge density $\rho_{\mathrm{M}}(\mathbf{P})$ [see Eq. (3)] of the same magnet A has not been considered. In relation to the point i), we note that by forcing the polarized sector E position (it has been assumed *a priori*), certain work depending on magnetic forces has to be done. Consequently, if E was free to rotate around its pin F, it would finish in a different position (an equilibrium position) from how *a priori* was fixed. The work needed to rotate the magnet E from the equilibrium position to the position fixed has not been considered. This work, in general, has to be furnished to the system.

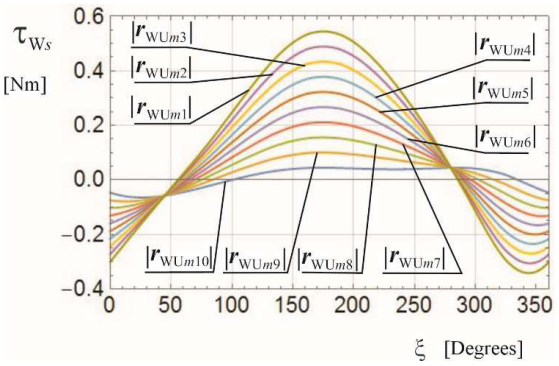

Figure 13. Modulus with the sign τ_{Ws} of the moment $\boldsymbol{\tau_{Ws}}$ applied to the moving set E-F-C along the tangent *s*-*s* (see Figure 9) versus ξ and $|\boldsymbol{r_{WUm}}|$.

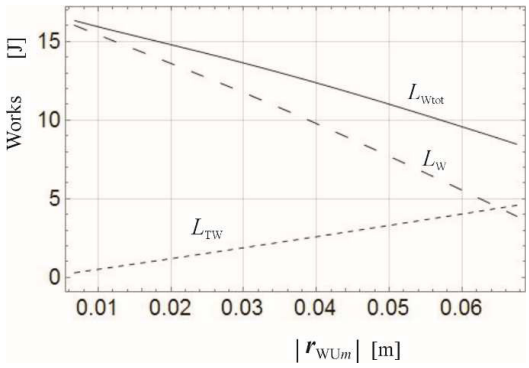

Figure 14. Works L_{W}, L_{TW}, and L_{Wtot} generated by the force $\mathbf{F_W}$, $\mathbf{F_{TW}}$, and $\mathbf{F_{Wtot}}$, respectively, versus $|\boldsymbol{r_{WUm}}|$.

Referring to point ii), if we do not consider the volume charge density, we disregard a certain contribution to the magnetic flux density. Therefore, the forces, moments and works associated with this contribution have not been taken into account. In this way we can justify the apparent energy generation of the system without using external energy sources.

7. CONCLUSIONS

An approach to computing forces, moments, and works in helical toroidal magnetic devices has been presented. The case study was developed with particular reference to a device constituted by permanent magnets, but the procedure illustrated to compute forces and moments is valid for whichever method is used to generate the magnetic flux density. Coils and currents (with or without permanent magnets) can be used to generate the magnetic inductance. The knowledge of forces and moments caused by this particular configuration of the magnetic field can be advantageous when searching for new configurations of electrical machines with high efficiency. In addition, the model illustrated can be useful to study the force applied to the conductors of machines like *tokamaks* and similar ones [7–18]. All the numerical computations of the present study have been performed by using the software MATHEMATICA 10.3 [31]. Further developments of this work will focus on the calculation of the forces, moments applied to the polarized sector E when the magnetic flux density is generated by an arrangement of plane magnet sectors with a constant magnetization vector $\mathbf{M}$ towards the relative thickness.This new arrangement of permanent magnets will be near to the helical toroidal shape of the magnet A illustrated in Figure 1. In this way it will be not necessary to consider the contribution of the volume charge density $\rho_{\mathrm{M}}(\mathbf{P})$ [see (3)] which, in the present study, has been disregarded. Moreover, for each position of the polarized sector E, the corresponding equilibrium around the pin F will be found. Therefore we will compute the new trends of the works L_{W}, L_{TW}, and L_{Wtot}.

APPENDIX A.

The analytical formulation for numerical computing of $\mathbf{B}_{\boldsymbol{Sa}}$ is described in detail in [6]. The formulation is based on the magnetic charge method. By applying this method, for simplicity, we neglect the contribution of the volume charge density ρ_{M}. We only consider the effect of the surface charge density σ_{M}. Denoting S_1 and S_2 the surfaces of the permanent magnet A indicated in Figure A1, related to the direction of the magnetization $\mathbf{M}$ of A, only these two surfaces give a contribution to the magnetic flux density $\mathbf{B}_{\boldsymbol{Sa}}$. The actual results are:

$$\sigma_{\mathrm{M1}}(\mathbf{P}) \cong M_x(\mathbf{P})n_{S1x}(\mathbf{P}) + M_y(\mathbf{P})n_{S1y}(\mathbf{P}) + M_z(\mathbf{P})n_{S1z}(\mathbf{P}), \tag{A1}$$

$$\sigma_{\mathrm{M2}}(\mathbf{P}) \cong M_x(\mathbf{P})n_{S2x}(\mathbf{P}) + M_y(\mathbf{P})n_{S2y}(\mathbf{P}) + M_z(\mathbf{P})n_{S2z}(\mathbf{P}), \tag{A2}$$

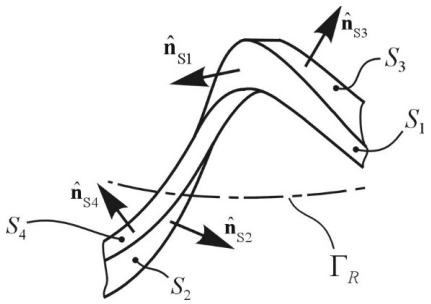

Figure A1. Helical toroidal surfaces S_1, S_2, S_3, and S_4 that bound the permanent magnet A [6].

$$\sigma_{\mathrm{M3}}(\mathbf{P}) \cong 0, \tag{A3}$$

$$\sigma_{\mathrm{M4}}(\mathbf{P}) \cong 0. \tag{A4}$$

$\sigma_{\mathrm{M1}}, \sigma_{\mathrm{M2}}, \sigma_{\mathrm{M3}}$, and σ_{M4} are the surface charge densities of the surfaces S_1, S_2, S_3, and S_4 of the magnet A, respectively. $\hat{\mathbf{n}}_{\boldsymbol{S1}}$, $\hat{\mathbf{n}}_{\boldsymbol{S2}}$, $\hat{\mathbf{n}}_{\boldsymbol{S3}}$, and $\hat{\mathbf{n}}_{\boldsymbol{S4}}$ are the normal versors at the generic point P of the infinitesimal surfaces dS_1, dS_2, dS_3, and dS_4, respectively. $\hat{\mathbf{n}}_{\boldsymbol{S1}}$ and $\hat{\mathbf{n}}_{\boldsymbol{S2}}$ are approximately parallel to the magnetization vector $\mathbf{M}$ of A (see Figure 1), while $\hat{\mathbf{n}}_{\boldsymbol{S3}}$ and $\hat{\mathbf{n}}_{\boldsymbol{S4}}$ are nearly perpendicular to $\mathbf{M}$=$\mathbf{M}(M_x, M_y, M_z)$. Consequently we obtain

$$\mathbf{B}_{\boldsymbol{S}}(\mathbf{P}') \cong \mathbf{B}_{\boldsymbol{S1}}(\mathbf{P}') + \mathbf{B}_{\boldsymbol{S2}}(\mathbf{P}') \tag{A5}$$

where [28]

$$\mathbf{B}_{\boldsymbol{S1}}(\mathbf{P}') = \frac{\mu_{\boldsymbol{0}}}{4\pi} \int_{S1} \frac{\sigma_{\mathrm{M1}}(\mathbf{P})(\mathbf{P}' - \mathbf{P})}{|\mathbf{P}' - \mathbf{P}|^3} dS \tag{A6}$$

and

$$\mathbf{B}_{\boldsymbol{S2}}(\mathbf{P}') = \frac{\mu_{\boldsymbol{0}}}{4\pi} \int_{S2} \frac{\sigma_{\mathrm{M2}}(\mathbf{P})(\mathbf{P}' - \mathbf{P})}{|\mathbf{P}' - \mathbf{P}|^3} dS \tag{A7}$$

In Eqs. (A5)–(A7) the vector $\mathbf{P}'$ identifies the generic point of S_a. By the same approach we compute $\mathbf{B}_{\boldsymbol{Sb}}$, whatever the position of S_a and S_b is. The vectors $\mathbf{B}_{\boldsymbol{Sa}}$ and $\mathbf{B}_{\boldsymbol{Sb}}$ evaluated at 625 points $\mathbf{P}'$ (end of $\mathbf{P}'$) of S_a and S_b are illustrated in Figure 10. The image shows 14 pairs of surfaces S_a and S_b and the relative magnetic inductions.

APPENDIX B.

This appendix contains explicit expressions for the parameters $\mathbf{b}$ and $\boldsymbol{r}_{\mathbf{W}}$ for computing the vector $\boldsymbol{r}'_{\mathbf{W}}$ defined by Eq. (38). With reference to Figure B1, the vector $\boldsymbol{r}$, whose modulus is $\boldsymbol{r}$ [see Figure 6(b)], is

$$\boldsymbol{r} = \boldsymbol{r}_{\mathbf{WU}\boldsymbol{m}} + \boldsymbol{r}_{\mathbf{W}}, \tag{B1}$$

from which we obtain

$$\boldsymbol{r}_{\mathbf{W}} = \boldsymbol{r} - \boldsymbol{r}_{\mathbf{WU}\boldsymbol{m}}. \tag{B2}$$

By considering a reference system $\mathrm{K}_m(X', Y', Z')$ integral to S_a [X' and Z' overlap with the tangent t_m-t_m and $\boldsymbol{r}_{\mathbf{WU}\boldsymbol{m}}$, respectively, Y' is perpendicular to X' and Z', see also Figure 6(a)], the moduli with the signs of the r components in such a system are

$$r_{x'} = r \sin\alpha, \tag{B3}$$

$$r_{y'} = 0, \tag{B4}$$

$$r_{z'} = r\cos\alpha - r_m, \tag{B5}$$

where

$$r_m = \frac{r_1 + r_2}{2} \tag{B6}$$

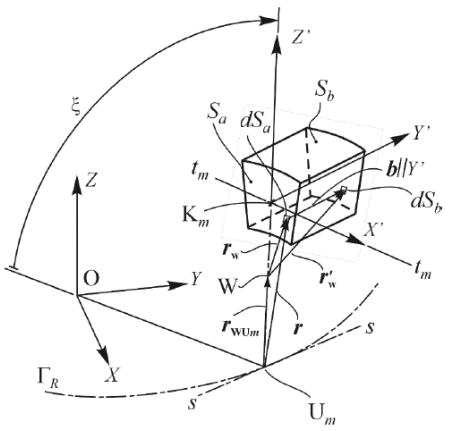

Figure B1. Definition of the vectors that identify the position of the infinitesimal surfaces dS_a and dS_b.

is the distance between the points U_m and K_m (see Figures B1 and 6). In the same $\mathrm{K}_m(X', Y', Z')$, the moduli with the signs of the r_{WUm} components are

$$r_{\mathrm{WU}mx'} = 0, \tag{B7}$$

$$r_{\mathrm{WU}my'} = 0, \tag{B8}$$

$$r_{\mathrm{WU}mz'} = r_{\mathrm{WU}m}. \tag{B9}$$

In Eq. (B9) $r_{\mathrm{WU}m}$ represents the modulus with the sign of the vector $\boldsymbol{r}_{\mathbf{WU}m}$. By Eqs. (B3)–(B9) and (B2), we obtain the moduli with the signs of the components of $\boldsymbol{r}_{\mathbf{W}}$ in the reference system $\mathrm{K}_m(X', Y', Z')$:

$$r_{\mathrm{W}x'} = r\sin\alpha, \tag{B10}$$

$$r_{\mathrm{W}y'} = 0, \tag{B11}$$

$$r_{\mathrm{W}y'} = r\cos\alpha - r_m - r_{\mathrm{WU}m}. \tag{B12}$$

By denoting (l_1, m_1, n_1), (l_2, m_2, n_2), and (l_3, m_3, n_3) the direction cosines of the X', Y', Z' axes relative to the X, Y, Z axes, respectively, we obtain the following moduli with the signs of the components of $\mathbf{r}_{\mathrm{W}}$ in the system $\mathrm{O}(X, Y, Z)$:

$$r_{\mathrm{W}x} = l_1 r_{\mathrm{W}x'} + l_2 r_{\mathrm{W}y'} + l_3 r_{\mathrm{W}z'}, \tag{B13}$$

$$r_{\mathrm{W}y} = m_1 r_{\mathrm{W}x'} + m_2 r_{\mathrm{W}y'} + m_3 r_{\mathrm{W}z'}, \tag{B14}$$

$$r_{\mathrm{W}z} = n_1 r_{\mathrm{W}x'} + n_2 r_{\mathrm{W}y'} + n_3 r_{\mathrm{W}z'}. \tag{B15}$$

By substituting (B10)–(B12) in (B13)–(B15), the final expressions of $r_{\mathrm{W}x}$, $r_{\mathrm{W}y}$, and $r_{\mathrm{W}z}$ are given by

$$r_{\mathrm{W}x} = l_1 r\sin\alpha + l_3(r\cos\alpha - r_m - r_{\mathrm{WU}m}), \tag{B16}$$

$$r_{\mathrm{W}y} = m_1 r\sin\alpha + m_3(r\cos\alpha - r_m - r_{\mathrm{WU}m}), \tag{B17}$$

$$r_{\mathrm{W}y} = n_1 r\sin\alpha + n_3(r\cos\alpha - r_m - r_{\mathrm{WU}m}). \tag{B18}$$

The direction cosines have to be evaluated versus the angle ξ, that is, $l_i = l_i(\xi)$, $m_i = m_i(\xi)$, and $n_i = n_i(\xi)$ with $i = 1, 2, 3$. Finally, we evaluate the moduli with sign of the $\mathbf{b}$ vector components. In the reference system $\mathrm{K}_m(X', Y', Z')$ the moduli with the signs are the following (see Figure B1):

$$b_{x'} = 0, \tag{B19}$$

$$b_{y'} = b, \tag{B20}$$

$$b_{z'} = 0. \tag{B21}$$

Therefore, the corresponding values in the $\mathrm{O}(X, Y, Z)$ are again obtained by using the direction cosines previously defined:

$$b_x = l_1 b_{x'} + l_2 b_{y'} + l_3 b_{z'}, \tag{B22}$$

$$b_y = m_1 b_{x'} + m_2 b_{y'} + m_3 b_{z'}, \tag{B23}$$

$$b_z = n_1 b_{x'} + n_2 b_{y'} + n_3 b_{z'}. \tag{B24}$$

By substituting (B19)–(B21) in the previous equations, we obtain

$$b_x = l_2 b, \tag{B25}$$

$$b_y = m_2 b, \tag{B26}$$

$$b_z = n_2 b. \tag{B27}$$

APPENDIX C.

In this appendix, we evaluate the angle ψ between the tangent t_{W}-t_{W} and the force $\mathbf{F}_{\boldsymbol{Sab}}$ applied by the magnet A to the magnet E (see Figures 7 and 1). By denoting the moduli with the signs w_x,w_y, and w_z of the versor of the tangent t_{W}-t_{W} to the toroidal helix Γ_{W} in W (see Figure 7), the angle ψ is given by the following equation

$$\psi = \arccos \frac{w_x F_{Sabx} + w_y F_{Saby} + w_z F_{Sabz}}{1 \cdot |\mathbf{F}_{\boldsymbol{Sab}}|}, \tag{C1}$$

where F_{Sabx}, F_{Saby}, and F_{Sabz}, are the moduli with the signs of the component of the force $\mathbf{F}_{\boldsymbol{Sab}}$. $|\mathbf{F}_{\boldsymbol{Sab}}|$ is the module of $\mathbf{F}_{\boldsymbol{Sab}}$ and the number "1" in the denominator of Eq. (B1) represents the module of the versor of t_{W}-t_{W}. $\mathbf{F}_{\boldsymbol{Sab}}$ is furnished by Eq. (16) and its components are known. Since w_x, w_y, w_z, F_{Sabx}, F_{Saby}, and F_{Sabz} depend on ξ, Eq. (C1) furnishes the function $\psi = \psi(\xi)$.

APPENDIX D.

In this appendix, we evaluate the angle $\psi_t(\xi)$ between the tangent t_{W}-t_{W} and the force $\mathbf{F}_{\mathbf{T}}$ (see Figure 9). ξ changes from 0 to 2π. We indicate $\hat{\mathbf{T}}$ the versor of the tangent t_{T}-t_{T} along which $\mathbf{F}_{\mathbf{T}}$ is applied. The moduli with the signs of the components of $\hat{\mathbf{T}}$ are (see Figure D1):

$$T_x = 1 \cdot \sin\xi \cos(\Delta_m + \frac{\xi\theta_p}{2\pi}), \tag{D1}$$

$$T_y = 1 \cdot \sin\xi \sin(\Delta_m + \frac{\xi\theta_p}{2\pi}), \tag{D2}$$

$$T_z = 1 \cdot \cos\xi. \tag{D3}$$

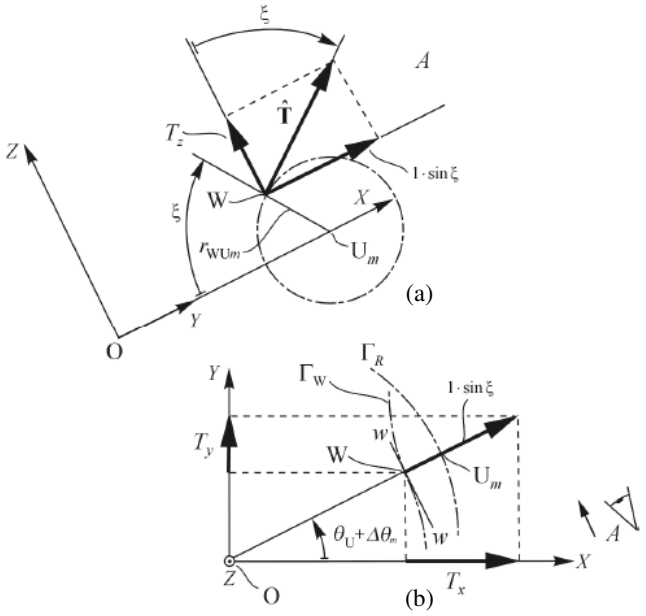

Figure D1. Components T_x, T_y, and T_z of the versor $\hat{\mathbf{T}}$.

The quantity $\frac{\xi\theta_p}{2\pi}$ in Eqs. (C1)–(C3) represents θ_{U} [see Eq. (23)]. Let us indicate $\hat{\mathbf{t}}_{\mathbf{W}}$ the versor of the tangent t_{W}-t_{W}. The moduli with the signs t_{W_x}, t_{W_y}, and t_{Wz} of the components of $\hat{\mathbf{t}}_{\mathbf{W}}$ are

$$t_{\mathrm{W}x} = \frac{x'_{\mathrm{W}}(\theta_{\mathrm{U}})}{\sqrt{x'_{\mathrm{W}}(\theta_{\mathrm{U}})^2 + y'_{\mathrm{W}}(\theta_{\mathrm{U}})^2 + z'_{\mathrm{W}}(\theta_{\mathrm{U}})^2}} \tag{D4}$$

$$t_{\mathrm{W}y} = \frac{y'_{\mathrm{W}}(\theta_{\mathrm{U}})}{\sqrt{x'_{\mathrm{W}}(\theta_{\mathrm{U}})^2 + y'_{\mathrm{W}}(\theta_{\mathrm{U}})^2 + z'_{\mathrm{W}}(\theta_{\mathrm{U}})^2}} \tag{D5}$$

$$t_{\mathrm{W}z} = \frac{z'_{\mathrm{W}}(\theta_{\mathrm{U}})}{\sqrt{x'_{\mathrm{W}}(\theta_{\mathrm{U}})^2 + y'_{\mathrm{W}}(\theta_{\mathrm{U}})^2 + z'_{\mathrm{W}}(\theta_{\mathrm{U}})^2}} \tag{D6}$$

where $x'_{\mathrm{W}}(\theta_{\mathrm{U}})$, $y'_{\mathrm{W}}(\theta_{\mathrm{U}})$, and $z'_{\mathrm{W}}(\theta_{\mathrm{U}})$ are the derivatives with respect to θ_{U} of the parametric equations $x_{\mathrm{W}}(\theta_{\mathrm{U}})$, $y_{\mathrm{W}}(\theta_{\mathrm{U}})$, and $z_{\mathrm{W}}(\theta_{\mathrm{U}})$ of Γ_{W} [see Eqs. (52)–(54)]. In Eqs. (D4)–(D5), again we substitute θ_{U} with $\frac{\xi\theta_p}{2\pi}$ and obtain $t_{\mathrm{W}x} = t_{\mathrm{W}x}(\xi)$, $t_{\mathrm{W}y} = t_{\mathrm{W}y}(\xi)$, and $t_{\mathrm{W}z} = t_{\mathrm{W}z}(\xi)$. The angle $\psi_t(\xi)$ is given by the following expression:

$$\psi_t = \arccos \frac{t_{\mathrm{W}x}T_x + t_{\mathrm{W}y}T_y + t_{\mathrm{W}z}T_z}{1 \cdot 1}. \tag{D7}$$

The product $1 \cdot 1$ in the denominator of Eq. (D7) underlines that the moduli of the two versors $\hat{\mathbf{T}}$ and $\hat{\mathbf{t}}_{\mathbf{W}}$ are equal to the unit value.

APPENDIX E. NOMENCLATURE

b thickness of the magnet E [see Figure 6(a)]
b vector that identifies the position of the surface dS_bstarting from the corresponding surface dS_a (the module of **b** is b)
B magnetic flux density
$\mathbf{B}_{\boldsymbol{Sa}}$ magnetic induction on the surface S_a
$\mathbf{B}_{\boldsymbol{Sb}}$ magnetic induction on the surface S_b
dL_{W} infinitesimal work generated by $\mathbf{F}_{\mathbf{W}}$ along the displacement $\mathbf{d\Gamma}_{\mathbf{W}}$
dL_{TW} infinitesimal work generated by $\mathbf{F}_{\mathbf{TW}}$ along the displacement $\mathbf{d\Gamma}_{\mathbf{W}}$
dL_{Wtot} infinitesimal work generated by $\mathbf{F}_{\mathbf{Wtot}}$ along the displacement $\mathbf{d\Gamma}_{\mathbf{W}}$
dS_a infinitesimal surface of the magnet E facing the magnet A
dS_b infinitesimal surface of the magnet E opposite to S_a
$\mathbf{d\Gamma}_{\mathbf{W}}$ infinitesimal displacement vector of the point W belonging to the toroidal helix Γ_{W}
$\mathbf{F}_{\boldsymbol{Sa}}$ force applied by the helical toroidal magnet A to the surface S_a
$\mathbf{F}_{\boldsymbol{Sb}}$ force applied by the helical toroidal magnet A to the surface S_b
$\mathbf{F}_{\boldsymbol{Sab}}$ resultant force applied to magnet E (see Figure 7)
$\mathbf{F}_{\mathbf{T}}$ force associated to the moment $\boldsymbol{\tau}_{\mathbf{W}\boldsymbol{s}}$
$\mathbf{F}_{\mathbf{TW}}$ component of $\mathbf{F}_{\mathbf{T}}$ along the tangent t_{W}-t_{W} to Γ_{W} at the point W (see Figure 9)
$\mathbf{F}_{\mathbf{W}}$ component of $\mathbf{F}_{\mathbf{Sab}}$ [see (15)] along the tangent t_{W}-t_{W} to Γ_{W} at the point W (see Figure 7)
$\mathbf{F}_{\mathbf{Wtot}}$ total force that pushes the parts E-F-C along the tangent t_{W}-t_{W} (see Figure 9)
F_{TW} modulus of $\mathbf{F}_{\mathbf{TW}}$
F_{W} modulus of $\mathbf{F}_{\mathbf{W}}$
F_{Wtot} modulus of $\mathbf{F}_{\mathbf{Wtot}}$
H magnetic field strength
L_{W} work developed by the force $\mathbf{F}_{\mathbf{W}}$ related to a complete rotation around the tangent s-s of the parts set E-F-C [see Figure 6(a)]
L_{TW} work developed by the force $\mathbf{F}_{\mathbf{TW}}$ related to a complete rotation around the tangent s-s of the parts set E-F-C [see Figure 6(a)]
L_{Wtot} work developed by the force $\mathbf{F}_{\mathbf{Wtot}}$ related to a complete rotation around the tangent s-s of the parts set E-F-C [see Figure 6(a)]
l_1, m_1, n_1 direction cosines of the X' axis integral to the magnet E and related to the X, Y, Z axes, respectively (see Figure B1)
l_2, m_2, n_2 direction cosines of the Y' axis integral to the magnet E and related to the X, Y, Z axes, respectively (see Figure B1)

l_3, m_3, n_3 direction cosines of the Z' axis integral to the magnet E and related to the X, Y, Z axes, respectively (see Figure B1)
$\mathbf{M}$ magnetization vector
M module of $\mathbf{M}$
$\hat{\mathbf{n}}$ normal versor to the surface on which $\sigma_{\mathrm{M}}(\mathbf{P})$ is defined
$\hat{\mathbf{n}}_a$ outgoing versor of the surface S_a
$\hat{\mathbf{n}}_b$ outgoing versor of the surface S_b
$\mathbf{P}$ vector that identifies a generic point P of a magnet
$\mathbf{P'}$ vector that identifies the point where the surface charge density is evaluated
r_1 internal radius of S_a and S_b
r_2 external radius of S_a and S_b
r_{G} radius of the torus illustrated in Figure 4(a)
r_m radius of the circular transversal section of the torus at which Γ belongs
$\boldsymbol{r_{\mathbf{W}}}$ vector that identifies the infinitesimal surface dS_a with respect to W [see Figure 6(b)]
$\boldsymbol{r_{\mathbf{WU}_m}}$ vector that identifies the point W from the point U_m [see Figure 6(b)
$|\boldsymbol{r_{\mathbf{WU}_m}}|$ modulus of $\boldsymbol{r_{\mathbf{WU}_m}}$
$\boldsymbol{r'_{\mathbf{W}}}$ vector that identifies the infinitesimal surface dS_b with respect to W [see Figure 6(b)]
R radius of Γ_R
S_a surface of the magnet E facing the magnet A
S_b surface of the magnet E opposite to S_a
x_{W},
y_{W},
z_{W} coordinates of the generic point W of Γ_{W}
$x'_{\mathrm{W}}(\theta_{\mathrm{U}})$ derivative of x_{W} with respect to θ_{U}
$y'_{\mathrm{W}}(\theta_{\mathrm{U}})$ derivative of y_{W} with respect to θ_{U}
$z'_{\mathrm{W}}(\theta_{\mathrm{U}})$ derivative of z_{W} with respect to θ_{U}
α, r polar coordinates that define the positions of dS_a and dS_b on S_a and S_b, respectively [see Figure 6(b) and 6(c)]
Γ barycentric curve of the helical toroidal surface of the magnet A facing the surface S_a (see Figure 1 and 5)
Γ_m helical toroidal curve coaxial to Γ_{W} [path of the point K_m (the barycentre of S_a), see Figures 4 and 6(a)]
Γ_R barycentric circumference of the helical toroidal screw B
Γ_{W} path generated by the point W [see Figure 4(a)]
$\Delta\theta_m$ rotation angle of Γ around the axis Z to generate Γ_m
ξ angle that identifies the position of S_a and S_b
θp angular extension measured in the plane that contains Γ_R of a coil of the magnet A [see Figures 6(a) and 6(c)]
θ_{U} angle that identifies the point U of Γ_R [see Figure 6(a)]
φ semiangle of the polarized angular sector E [see Figures 6(a) and 6(c)]
$\rho_{\mathrm{M}}(\mathbf{P})$ volume charge density
$\sigma_{\mathrm{M}}(\mathbf{P})$ surface charge density
$\sigma_{\mathrm{M}_a}(\mathbf{P'})$ surface charge density of the surface S_a
$\sigma_{\mathrm{M}_b}(\mathbf{P'})$ surface charge density of the surface S_b
$\boldsymbol{\tau_{\mathbf{S}a\mathbf{W}}}$ moment generated from $\mathbf{F}_{\boldsymbol{S}a}$ and applied to the parts E, F, and C
$\boldsymbol{\tau_{\mathbf{S}a\mathbf{W}s}}$ component of $\boldsymbol{\tau_{\mathbf{S}a\mathbf{W}}}$ along the tangent s-s (see Figure 4(b))]
$\boldsymbol{\tau_{\mathbf{W}}}$ resultant moment applied to the moving magnet E, the pin F, and the lobed ring C with respect the point W [see Figures 1–3, 4(b)
$\boldsymbol{\tau_{\mathbf{W}s}}$ component of $\boldsymbol{\tau_{\mathbf{W}}}$ along the tangent s-s to the circumference Γ_R in U_m (see Figure 8)
ψ angle between $\mathbf{F}_{\boldsymbol{S}ab}$ and the tangent t_{W}-t_{W} (see Figure 7)
ψ_t angle between the direction of $\mathbf{F}_{\mathbf{T}}$ and t_{W}-t_{W} (see Figure 9)

APPENDIX F. SUPPLEMENTARY MATERIALS

The numerical implementation concerning the *Mathematica* programming is available (please contact the author at muscia@units.it).

REFERENCES

1. Vanoost, D., H. De Gersem, J. Peuteman, G. Gielen, and D. Pissoort, "Nonlinear magnetostatic finite element formulation for models with radial symmetry," *IEEE Transactions on Magnetics*, Vol. 50, No. 3, Febraury 2014.
2. Štumberger,B., G. Štumberger, D. Dolinar, A. Hamler, and M. Trlep, "Evaluation of saturationand cross-magnetization effects in interior permanent-magnet synchronous motor," *IEEE Transactions on Industry Applications*, Vol. 39, No. 5, 1264–1271, September/October 2003.
3. Štumberger, B., G. Štumberger, and D. Dolinar, "Analysis of cross-saturation effects in a linear synchronous reluctance motor performed by finite elements method and measurements," *Proceedings of 12th International Conference on Power Electronics and Motion Control, EPE-PEMC 2006*, IEEE Conferences Publications, 2006.
4. Ruoho, S. and A. Arkkio, "Partial demagnetization of permanent magnets in electrical machines causedby an inclined field," *IEEE Transactions on Magnetics*, Vol. 44, No. 7, 1773–1778, July 2008.
5. Fratila, R., A. Benabou, A. Tounzi, and J. C. Mipo, "Nonlinear modeling of magnetization loss in permanent magnets," *IEEE Transactions on Magnetics*, Vol. 48, No. 11, 2957–2960, November 2012.
6. Muscia, R., "Symmetry of magnetostatic fields generated by toroidal helicoidal magnets," *IEEE Transactions on Magnetics*, Vol. 51, No. 10, 7002614, October 2015.
7. Brouver, L., S. Caspi, D. Robin, and W. Wan, "3D toroidal field multipoles for curved accelerator magnets," *Proceedings of PAC 2013*, 907–909, Pasadena, CA, USA, 2013.
8. He, Y., Z. Yang, W. Ba, X. Zhang, G. Zhuang, X. Hu, Y. Pan, and Z. Liu, "Calculation of the poloidal magnetic field configuration for the J-TEXT tokamak," *IEEE Transactions on Applied Superconductivity*, Vol. 20, No. 3, 1840–1843, 2010.
9. Maviglia, F., R. Albanese, M. De Magistris, P. J. Lomas, S. Minucci, F. G. Rimini, A. C. C. Sips, and P. C. De Vries, "Electromagnetic models of plasma breakdown in the JET tokamak," *IEEE Transactions on Magnetics*, Vol. 50, No. 2, Febraury 2014.
10. Jin, C. G., T. Yu, Y. Zhao, Y. Bo, C. Ye, J. S. Hu, L. J. Zhuge, S. B. Ge, X. M. Wu, H. T. Ji, and J. G. Li, "Helicon plasma discarge in a toroidal magnetic field of the tokamak," *IEEE Transactions on Plasma Science*, Vol. 39, No. 11, 3103–3107, November 2011.
11. Albanese, R., G. Artaserse, F. Maviglia, F. Piccolo, and F. Sartori, "Identification of vertical instabilities in the JET tokamak," *IEEE Transactions on Magnetics*, Vol. 44, No. 6, June 2008.
12. Albanese, R., M. De Magistris, R. Fresa, F. Maviglia, and S. Minucci, "Numerical formulations for accurate magnetic field flow tracing in fusion tokamaks," *Proceedings of the 9th International Conference on Computation in Electromagnetics (CEM 2014)*, DOI: 10.1049/cp. 2014.0211, 2014.
13. Beidler, D. C., E. Harmeyer, F. Herrnegger, J. Kisslinger, Y. Igitkhanov, and H. Wobig, "Stellarator fusion reactors — An overview," *Proceedings of Toki Conference ITC12*, December 2001.
14. Probert, P., "High-performance interpolation of stellarator magnetic fields," *IEEE Transactions on Plasma Science*, Vol. 39, No. 4, 1051–1054, April 2011.
15. Neilson, G. H., D. A. Gates, P. J., Heitzenroeder, S. C. Prager, T. Stevenson, P. Titus, M. D. Williams, and M. C. Zarnstorff, "Facilities for Quasi-Axisymmetric Stellarator research," *Proceedings of 25th Symposium on Fusion Engineering (SOFE)*, 2013 IEEE Conferences Publications, 2013.
16. Imagawa, S., A. Sagara, and Y. Kozaki, "Conceptual design of magnets with CIC conductors for LHD-type reactors FFHR2m," *Plasma and Fusion Research*, Vol. 3, S1050, 1–5, 2008.
17. Rummel, T., K. Riβe, G. Ehrke, K. Rummel, A. John, T. Mönnich, K. P. Buscer, W. H. Fietz, R. Heller, O. Neubauer, and A. Panin, "The superconducting magnet system of the stellarator wendlstein 7-X," *IEEE Transactions on Plasma Science*, Vol. 40, No. 3, 769–776, March 2012.
18. Clark, A. W., F. A. Volpe, and D. A. Spong, "Proto-circus tilted-coil tokamak-stellarator hybrid," *Proceedings of 25th Symposium on Fusion Engineering (SOFE)*, 2013 IEEE Conferences Publications, 2013.

19. Dal Maso, A., "Screws with curvilinear axis: A CAD analysis of coupling problems," *Thesis*, Supervisor: R. Muscia, Department of Engineering and Architecture, University of Trieste, Italy, 2014.
20. Chen, M., K. T. Chau, C. H. T. Lee, and C. Liu, "Design and analysis of a new axial-field magnetic variable gear using pole-changing permanent magnets," *Progress In Electromagnetics Research*, Vol. 153, 23–32, 2015.
21. Boutora, Y., N. Takorabet, and R. Ibtiouen, "Analytical model on real geometries of magnet bars of surface permanent magnet slotless machine," *Progress In Electromagnetics Research B*, Vol. 66, 31–47, 2016.
22. Sun, X., S. Luo, L. Chen, R. Zhao, and Z. Yang, "Suspension force modelling and electromagnetic characteristics analysis of an interior bearingless permanent magnet synchronous motor," *Progress In Electromagnetics Research B*, Vol. 69, 31–45, 2016.
23. Brown, Jr., W. F., "Electric and magnetic forces: A direct calculation I," *Am. J. Phys.*, Vol. 19, 290–304, 1951.
24. Brown, Jr., W. F., "Electric and magnetic forces: A direct calculation II," *Am. J. Phys.*, Vol. 19, 333–350, 1951.
25. Muscia, R., "Equivalent magnetic charge in helicoidal magnets," *J. Appl. Phys.*, Vol. 104, 103916, 2008.
26. Muscia, R., "Computation of the magnetic field generated by helical toroidal permanent magnets," *Electromagnetics*, Vol. 32, 8–30, 2012.
27. Furlani, E. P., *Permanent Magnet and Electromechanical Devices, Material, Analysis, and Applications*, 136, Eq. (3.118), Academic Press, 2001.
28. Furlani, E. P., "A formula for the levitation force between magnetic disks," *IEEE Transactions on Magnetics*, Vol. 29, No. 6, 4165–4169, November 1993.
29. Furlani, E. P., "Formulas for the force and torque of axial coupling," *IEEE Transactions on Magnetics*, Vol. 29, No. 5, 2295–2301, September 1993.
30. Furlani, E. P., R. Wang, and H. Kusnadi, "A three-dimensional model for computing the torque of radial couplings," *IEEE Transactions on Magnetics*, Vol. 31, No. 5, 2522–2526, September 1995.
31. *Mathematica 10.3*, [Online] Available: http://www.wolfram.com/mathematica.